



HAL
open science

Transformation of Co-containing birnessite to todorokite: Effects of Co on the transformation and implications for Co mobility

Zhongkuan Wu, Caroline L. Peacock, Bruno Lanson, Hui Yin, Lirong Zheng, Zhongjun Chen, Wenfeng Tan, Guohong Qiu, Fan Liu, Xionghan Feng

► To cite this version:

Zhongkuan Wu, Caroline L. Peacock, Bruno Lanson, Hui Yin, Lirong Zheng, et al.. Transformation of Co-containing birnessite to todorokite: Effects of Co on the transformation and implications for Co mobility. *Geochimica et Cosmochimica Acta*, 2019, 246, pp.21-40. 10.1016/j.gca.2018.11.001 . insu-03022652

HAL Id: insu-03022652

<https://insu.hal.science/insu-03022652>

Submitted on 24 Nov 2020

HAL is a multi-disciplinary open access archive for the deposit and dissemination of scientific research documents, whether they are published or not. The documents may come from teaching and research institutions in France or abroad, or from public or private research centers.

L'archive ouverte pluridisciplinaire **HAL**, est destinée au dépôt et à la diffusion de documents scientifiques de niveau recherche, publiés ou non, émanant des établissements d'enseignement et de recherche français ou étrangers, des laboratoires publics ou privés.

18 Abstract

19 The mobility and fate of bioessential transition metals, such as Ni and Co, are
20 strongly controlled by their association with phylломanganate minerals such as
21 birnessite. These minerals however, can transform to tectomanganates such as
22 todorokite during soil and sediment diagenesis, yet the mobility and fate of most
23 metals during the transformation process remain largely unknown. Here this research
24 investigates the effect of Co on, and the mobility and fate of Co during the
25 transformation of birnessite into tunnel structure minerals. A range of Co-containing
26 birnessite precursors with up to 20% Co/(Co+Mn) molar ratios were synthesised, and
27 subsequently transformed via a mild reflux procedure designed to mimic the
28 diagenesis of these layered precursors into tunnel structures. The layered precursors
29 and reflux products were characterized using a combination of mineralogical and
30 geochemical techniques, including powder X-ray diffraction (XRD), Fourier
31 transform infrared spectroscopy (FTIR), high resolution transmission electron
32 microscopy (HRTEM) and extended X-ray absorption fine structure (EXAFS)
33 spectroscopy. The results show that Co(III) is structurally incorporated into the
34 layered precursors and reflux products, through the isomorphic substitution of Mn(III).
35 The structural incorporation of Co(III) into the layered precursors leads to an overall
36 reduction of Jahn-Teller distorted Mn(III) octahedra in these minerals, a key factor for
37 their transformation to tunnel structures. As a consequence, the presence of such
38 structural Co(III) disrupts the transformation of birnessite into todorokite, leading to
39 the coexistence of 9.6 Å asbolane-like phylломanganate and non-ideal $3 \times n$, or
40 α -disordered, todorokite-like tectomanganates in the transformation products. Newly
41 formed todorokite exhibits a wide range of $3 \times n$ tunnel dimensions (n up to 13) and a
42 plate-like morphology. Overall the structural incorporation of non Jahn-Teller
43 distorted cations like Co(III) into birnessite might help explain the often observed
44 predominance of phylломanganates over tectomanganates in soils and sediments, and
45 the persistence of phylломanganates in ferromanganese deposits that can be many

46 millions of years old. The results also indicate that Co(III) initially associated with
47 birnessite is retained in the solid phase during transformation, and thus the mobility of
48 Co(III) is limited. EXAFS data suggest that Co is mainly located in the octahedral
49 layers of asbolane-like phyllosulfate and at non-edge sites in non-ideal todorokite.
50 Overall the transformation of Co-containing birnessite into non-ideal todorokite and
51 asbolane-like layered structures maintains the strong sequestration of Co by Mn
52 oxides.

53

54 *Keywords:* layered Mn oxide precursor; birnessite; tunnel structure; todorokite; XRD;
55 EXAFS; nitric acid treatment

56

57

1. INTRODUCTION

58 Natural Mn oxides encompass a variety of structural variants, most of them based
59 on Mn(III, IV)O₆ octahedra sharing edges and/or corners (Post, 1999). These oxides
60 are ubiquitous, occurring for example in soils, sediments and oceanic ferromanganese
61 crusts and nodules (Taylor et al., 1964; Burns and Burns, 1975, 1977; Chukhrov et al.,
62 1982; Murray et al., 1984; Post, 1999; Vodyanitskii et al., 2004). The coexistence of
63 Mn(II/III/IV) within these oxides, and the related charge deficit that this creates,
64 makes these oxides highly reactive, in particular with respect to the sorption and/or
65 oxidation of transition metals (e.g., Manceau et al. 2002; Tebo et al., 2004; Webb et al.,
66 2005; Peacock and Sherman, 2007a; Peacock, 2009;) and the oxidative degradation of
67 organic contaminants (Tebo et al., 2004; Remucal and Ginder-Vogel, 2014). The
68 reactivity of these oxides is often reinforced by their micro- to nano-crystallinity,
69 which provides them with large specific surface areas (Post, 1999; Lanson et al., 2000,
70 2002a,b). This strengthens their role as key players in the environmental fate of
71 inorganic and organic nutrients and contaminants (e.g., Villalobos et al., 2005;
72 Lafferty et al., 2010; Grangeon et al., 2012), but in turn often hampers their precise
73 identification (Chukhrov et al., 1987; Post, 1999).

74 Two main families of Mn oxides may be differentiated, i.e. phylломanganates and
75 tectomanganates. Phylломanganates are 2D minerals whose layers are built of
76 edge-sharing MnO₆ octahedra. Layer charge deficit results either from isomorphic
77 Mn(III)-for-Mn(IV) substitutions or from the presence of vacant layer sites. In the
78 first instance, to minimize steric strains arising from the Jahn-Teller distortion of
79 Mn(III) octahedra, these elementary blocks may be segregated into Mn(III)-rich rows
80 in which the octahedra are systematically elongated along the same direction (the *a*
81 axis). The induced cooperative Jahn-Teller effect then leads to an orthogonal layer
82 symmetry ($a > \sqrt{3}b$), and the layer charge deficit is generally compensated for by the
83 presence of protons, hydrated alkali or alkaline-earth cations (Drits et al., 1997, 2007;
84 Silvester et al., 1997, Lanson et al., 2002a; Webb et al., 2005; Gaillot et al., 2007). In
85 the second instance, the presence of vacant layer sites leads to a hexagonal layer
86 symmetry ($a = \sqrt{3}b$), where the layer charge deficit is neutralized by interlayer cations
87 such as H⁺, K⁺, and so on (Silvester et al., 1997; Manceau et al., 1997; Lanson et al.,
88 2000; Villalobos et al., 2006; Bodeř et al., 2007; Drits et al., 2007; Peacock and
89 Sherman, 2007b). The vacant layer sites also allow for the sorption of multi-valent
90 cations as inner sphere complexes above/below these sites (triple corner sites: e.g.,
91 Post and Appleman, 1988; Manceau et al., 1997, 2002, 2004, 2007; Lanson et al.,
92 2002b; Villalobos et al., 2005; Peacock and Sherman, 2007a, b; Grangeon et al., 2008;
93 Peacock, 2009; Peña et al., 2010). In both orthogonal and hexagonal
94 phylломanganates, the layer-to-layer distance is ~7.0-7.2 Å (e.g. birnessite, vernadite,
95 chalcophanite; Post and Appleman, 1988; Drits et al., 1997; Silvester et al., 1997;
96 Lanson et al., 2000, 2002a,b). This distance may be increased to ~9.4-10.0 Å when
97 interlayer alkali or alkaline-earth cations retain two planes of interlayer H₂O
98 molecules (i.e. busserite) or when an additional octahedral brucite-like sheet is
99 sandwiched between two Mn octahedral sheets (lithiophorite, asbolane; Chukhrov et
100 al., 1982, 1987; Manceau et al., 1987; Post and Appleman, 1988, 1994; Post, 1999).

101 Tectomanganates are 3D minerals, in which chains of edge-sharing MnO₆

102 octahedra share corners, thus leading to “tunnel” structures. Nomenclature of the
103 natural tunnel oxides relies essentially on the $n \times m$ tunnel size, with ideal pyrolusite,
104 cryptomelane and todorokite having 1×1 , 2×2 and 3×3 tunnel sizes, respectively, and
105 on the nature of the cations present within these tunnels. It is commonly accepted that
106 tectomanganates originate from the transformation of phylломanganate precursors
107 (Burns and Burns, 1977; Golden et al., 1986; Ching et al., 1999; Feng et al., 1999;
108 Shen et al., 2005; Bodeř et al., 2007; Cui et al., 2008, 2009, 2010; Grangeon et al.,
109 2014, 2015; Atkins et al., 2014). For example, todorokite, that exhibits intense
110 diffraction lines at 9.6 Å and 4.8 Å (JCPDS 38-0475), may be prepared by heating
111 Mg-exchanged buserite either in an autoclave or at atmospheric pressure (Golden et
112 al., 1986; Feng et al., 2004). As phylломanganate precursors often have transition
113 metals sorbed at their surface and/or incorporated within their octahedral layers, the
114 fate of these elements during the phylломanganate-to-tectomanganate conversion is of
115 special interest for their geochemical cycling (e.g., Siegel and Turner, 1983; Atkins et
116 al., 2014, 2016). Experimental investigations of the mobility and fate of metals during
117 todorokite formation from layered precursors however, show mixed results, with
118 studies reporting both the incorporation of metal ions into the framework of newly
119 formed todorokite (Yin et al., 1994; Ching et al., 1999; Nicolas-Tolentino et al., 1999;
120 Kumagai et al., 2005; Onda et al., 2007) or the loss of metal ions from precursor
121 birnessite with only the surface adsorption of metal ions onto newly formed
122 todorokite (Atkins et al., 2016).

123 In this context, the fate of Co during the transformation of layered precursors is of
124 special interest owing to its high natural affinity for layered Mn oxides. Early
125 observations showed that layered Mn minerals present in Australian soils (birnessite
126 and lithiophorite) contain relatively large amounts of Co with Co/(Co+Mn) molar
127 ratios of ~0.01-0.02 (Taylor et al., 1964; Taylor, 1968). Similarly, in mining district
128 sediments Co concentration is also positively correlated with the content of Mn oxides
129 (Fuller and Harvey, 2000; Dublet et al., 2017), which can exhibit Co/(Mn+Co) molar

130 ratios up to 0.34 (asbolane; [Manceau et al., 1987](#)). This geochemical Mn-Co
131 association is also recognized in the marine environment, where ferromanganese
132 nodules and crusts composed predominantly of layered Mn oxides are enriched in Co
133 relative to seawater (e.g., [Murray, 1975](#); [Burns and Burns, 1977](#); [Murray and Dillard,
134 1979](#); [Saito et al., 2002](#)). Monomineralic Co-containing layered Mn oxides, such as
135 lithiophorite and asbolane, have been identified in soils, lateritic formations and
136 oceanic ferromanganese nodules ([Chukhrov et al. 1982, 1987](#); [Ostwald, 1984](#); [Llorca,
137 1987, 1988](#); [Manceau et al. 1987, 1992](#)). Coupled with Co sorption, layered Mn
138 oxides are also able to oxidize Co(II). The oxidation of Co(II)-to-Co(III) by birnessite
139 was first revealed using X-ray photoelectron spectroscopy ([Murray and Dillard, 1979](#)),
140 and later shown to be initiated at the edges of birnessite particles ([Simanova and Peña,
141 2015](#)). A combination of polarized extended X-ray absorption fine structure (EXAFS)
142 spectroscopy and X-ray diffraction (XRD) shows that both layer and interlayer Mn(III)
143 can oxidize Co(II) and lead to Co(III) migration into the octahedral layers ([Manceau
144 et al., 1997](#); [Yu et al., 2012](#)). Both Co(II) oxidation and the subsequent migration of
145 Co(III) into the mineral structure appear to be key to the high capacity of layered Mn
146 oxides for Co scavenging ([Yin et al., 2014](#)) and their resulting Co-enrichment
147 ([Loganathan and Burau, 1973](#); [Davies and Morgan, 1989](#)). As Co(III)O₆ octahedra are
148 not Jahn-Teller distorted, Co-enrichment in birnessite layers may modify layer
149 symmetry from orthogonal to hexagonal ([Yin et al., 2015](#)). This enrichment may also
150 impact the ability of Co-containing phyllosulfates to transform into
151 tectomanganates as the abundance of distorted Mn(III) octahedra within the
152 octahedral layers appears to be a key factor for the formation of tunnel structures
153 ([Burns et al., 1985](#); [Bodei et al., 2007](#); [Cui et al., 2008](#); [Atkins et al., 2014, 2016](#);
154 [Grangeon et al., 2014, 2015](#); [Zhao et al., 2015](#)).

155 To the authors' knowledge only a handful of studies have investigated the
156 transformation of Co-containing layered Mn oxides into tunnel structures ([Ching et al.,
157 1999](#); [Kumagai et al., 2005](#); [Onda et al., 2007](#); [Song et al., 2010](#)). As expected, Co(II)

158 is oxidized to Co(III) in the layered precursors and then indirect observations indicate
159 that a significant proportion of Co in the precursor can be structurally incorporated
160 into the newly formed tunnel structures, by replacing Mn (Ching et al., 1999;
161 Kumagai et al., 2005; Onda et al., 2007; Song et al., 2010). In particular, it is
162 suggested that Co(III) primarily substitutes for Mn(III) at the edge sites (Mn²⁺ and
163 Mn⁴⁺, Fig. 1) of the 3×3 tunnel structure (Song et al., 2010). However, the mechanism
164 of Co retention and the extent to which precursor Co is retained in the newly formed
165 products are still unclear, and thus the mobility and fate of Co during the birnessite to
166 todorokite transformation are still unknown.

167 The present study explores the transformation of Co-containing layered Mn oxide
168 precursors into tectomanganates, in order to investigate the effect of Co on, and the
169 fate of Co during the transformation process. A combination of XRD,
170 Fourier-transform infrared (FTIR) spectroscopy, nitric acid treatment and
171 high-resolution transmission electron microscopy (HRTEM) are used to characterize
172 the layered precursors and the transformation products, and determine the effect of Co
173 on their structures. The effect of Co on the transformation process is investigated and
174 the key parameters leading to the formation of layered vs. tunnel structures are
175 determined. These techniques are then combined with X-ray absorption near-edge
176 structure (XANES) and EXAFS spectroscopy to examine the Mn and Co crystal
177 chemistry in the layered precursors and transformation products, in order to better
178 understand the ultimate fate of Co during layered Mn oxide transformation.

179

180 **2. EXPERIMENTAL METHODS**

181 **2.1. Synthesis of layered precursors and transformation products**

182 A number of different Co-containing layered precursors (birnessite) and
183 transformation products were prepared after Feng et al. (2004) and Song et al. (2010),
184 together with Co-free birnessite and todorokite reference materials. To prepare the
185 layered precursors, 250 mL of 5.5 M NaOH solution (refrigerated for 5 h at 4 °C) was

186 added quickly to a 200 mL solution containing 0.5 M (Mn(II)+Co(II)), as MnCl₂ and
187 CoCl₂, in which the molar ratios of Co to (Mn+Co) were 0, 0.05, 0.10, 0.15 and 0.20.
188 The mixed solution was then stirred vigorously for 5 h and aerated with 2 L/min O₂.
189 Each precipitate was washed with deionized water until the conductivity was below 2
190 μS/cm and half of each precipitate was dried at 60 °C for 3 days, while the other half
191 was used to prepare todorokite. Layered precursors with molar ratios of Co/(Mn+Co)
192 of 0, 0.05, 0.10, 0.15 and 0.20 are named Bir, CoB5, CoB10, CoB15 and CoB20,
193 respectively, and the Co-containing layered precursors are collectively referred to as
194 CoB.

195 The transformation of the layered precursors into tectomanganates was achieved
196 using a reflux process (Feng et al., 2004). Briefly, the wet layered precursor was
197 dispersed in 400 mL of 1 M MgCl₂ solution, stirred for 12 h at room temperature, and
198 then washed 3 times. The resulting wet slurry was re-suspended in 500 mL deionized
199 water in a 1 L triangle flask connected to a glass condenser with an oil bath kept at
200 100 °C and stirred for 24 h. After cooling to room temperature, the reflux products
201 were separated from the solution by filtration, washed 3 times with deionized water
202 and dried at 60 °C for 3 days. Transformation products of Bir, CoB5, CoB10, CoB15
203 and CoB20 are named Tod, CoT5, CoT10, CoT15 and CoT20, respectively, and the
204 Co-containing reflux products are collectively referred to as CoT.

205 After the reflux procedure and when the reflux solutions were at room temperature
206 (23 °C), the conductivity of these solutions was measured with a LeiCi DDS-11A
207 conductimeter. All solid samples were ground in an agate mortar to particle sizes
208 below 100 micron mesh to perform measurements described in Section 2.2. The
209 elemental composition of all solid samples was determined in triplicate via atomic
210 absorption spectrometry (Varian AAS 240FS). Actual Co/(Mn+Co) mole ratios in the
211 Co-containing birnessites and reflux products are shown in Table 1. Co K-edge X-ray
212 absorption near edge structure (XANES) spectra that confirm the presence of Co(III)
213 in the layered precursors and reflux products are shown in Figure S1 (Supplementary

214 Information).

215

216 **2.2 Characterization of layered precursors and reflux products**

217 The mineralogy of all samples was determined by powder XRD, collected on a
218 Bruker D8 Advance diffractometer with Cu K α radiation ($\lambda=0.15418$ nm), operated at
219 40 kV/40 mA and at a scan rate of 1 °/min with a 0.02 ° step. FTIR spectroscopy was
220 also performed, using a Bruker VERTEX 70. Prior to spectra acquisition, samples
221 were mixed with KBr in a 1:80 ratio and then pressed into transparent slices. Spectra
222 were recorded over 4000-400 cm⁻¹ with a resolution of 1 cm⁻¹ and with an average of
223 64 scans per sample (Zhao et al., 2015). Because it can be difficult to distinguish
224 tectomanganate from busserite, lithiophorite- or asbolane-like phases using XRD (e.g.,
225 Burns et al., 1983, 1985; Bodeř et al., 2007; Saratovsky et al., 2009; Feng et al., 2010)
226 we also performed a non-reducing nitric acid wash. This acid wash removes
227 exchangeable species present in the interlayers of phyllomanganates and the tunnels
228 of tectomanganates and so together with XRD provides information on mineral
229 composition and structure. Specifically, after the loss of exchangeable species the
230 d-spacing of phyllomanganates decreases from ~10 Å to ~7 Å, while that of
231 todorokite remains stable. The acid wash also removes sorbed species and therefore
232 the composition of the wash solution provides information on the crystal chemistry of
233 Mn and Co, for example, whether Co is sorbed or structurally incorporated. The acid
234 wash was conducted by adding 0.1 g sample into 250 mL 1 M HNO₃ solution with
235 moderate stirring at room temperature (20 °C). An aliquot of 5 mL of the mixtures
236 was withdrawn at different time intervals and immediately filtered through a 0.22 μm
237 membrane to investigate the release of Mg, Mn and Co, the contents of which were
238 analyzed by atomic absorption spectrometry.

239 The specific surface area of the reflux products was determined by the
240 Brunauer–Emmett–Teller (BET) method using an Autosorb-1 standard physical
241 adsorption analyzer (Quantachrome Autosorb-1, JEDL-6390/LV). Briefly, 0.15 g of

242 sample was degassed at 110 °C for 3 h under vacuum prior to N₂ adsorption. The
243 micromorphology of the reflux products was imaged with HRTEM on a Jeol
244 JEM2100F operated at 200 kV.

245 The Mn and Co local environments in the layered precursors and reflux products
246 were investigated using Mn and Co K-edge EXAFS spectroscopy. Spectra were
247 collected at room temperature on the 1W1B beamline of the Beijing Synchrotron
248 Radiation Facility (BSRF). Data were recorded in transmission mode (Mn K-edge) or
249 fluorescence yield mode (Co K-edge), and the spectrum of a metallic Mn or Co foil
250 was acquired simultaneously in transmission mode as a reference for energy
251 calibration, respectively. The EXAFS spectra were processed via Athena, and fit using
252 Artemis (Ravel and Newville, 2006). The Mn spectra were fit in R-space (R+ΔR)
253 from 1 to 4 Å (3.06–12.7 Å⁻¹), with an amplitude reduction factor (S_0^2) of 0.8
254 (Grangeon et al., 2010). The Co spectra were also fit in R-space (R+ΔR) from 1 to 4
255 Å (3.2–11.5 Å⁻¹), with an amplitude reduction factor (S_0^2) of 0.973 (Yin et al., 2014,
256 2015). Both the Mn and Co K-edge fits used scattering paths calculated from Mn/Co
257 atoms in the Mn2 site in todorokite (JCPDS 38-0475), which contains both edge- and
258 corner-sharing linkages. The Mn K-edge EXAFS spectra were also fit in Athena to
259 determine the proportions of 9.6 Å phylломanganate and tectomanganate in the reflux
260 products. To do this, linear combination fitting of Mn K-edge EXAFS spectra was
261 performed from 3 to 12 Å⁻¹, using CoT5 and corresponding CoB as standard samples
262 for Co-containing tunnel and layered structures.

263 The Mn average oxidation state (AOS) in the layered precursors and reflux
264 products was determined by applying a linear combination fitting method to the Mn
265 K-edge XANES data, that is specifically designed for the determination of Mn
266 valence states in mixed-valent Mn oxides (the so-called Combo method; Manceau et
267 al., 2012). The reference compounds used for Mn(II), Mn(III) and Mn(IV) were those
268 used in the original study (Manceau et al., 2012; Table 1).

269

3. RESULTS

3.1 Mineralogy of layered precursors and reflux products

3.1.1 X-ray diffraction

Birnessite has basal reflections at ~ 7.2 Å (001) and ~ 3.6 Å (002) (see triclinic birnessite JCPDS 43-1456 and hexagonal birnessite JCPDS 23-1239), while for the equivalent layered precursor with an expanded interlayer these appear at ~ 9.6 Å (001) and ~ 4.8 Å (002) (see busserite JCPDS 32-1128). Both birnessite and busserite also have hk reflections/bands at ~ 2.4 Å and ~ 1.4 Å due to periodicities within the phyllomanganate layers. In common with ~ 9.6 Å phyllomanganate, the tectomanganate todorokite has peaks at ~ 9.6 Å (001/100), ~ 4.8 Å (002/200), ~ 2.4 – 2.5 Å (21-1)/(40-1) and (210), and ~ 1.4 Å (020) (see JCPDS 38-475). As such, it can be difficult to distinguish todorokite from ~ 9.6 Å phyllomanganate using XRD (e.g., Burns et al., 1983, 1985; Bodeř et al., 2007; Saratovsky et al., 2009; Feng et al., 2010). However, in contrast to ~ 9.6 Å phyllomanganate, todorokite has additional peaks at 2.21 Å (21-2), 1.95 Å (21-3), 1.73 Å (313) and 1.52 Å (21-5) (see JCPDS 38-475). In addition, when ~ 9.6 Å layered precursors and todorokite reflux products are mixed, the ~ 2.4 Å peak is prominent and the ~ 2.5 Å peak manifests as a splitting of the ~ 2.4 Å peak (Atkins et al., 2014).

The XRD pattern of Bir (Fig. 2a) is in good agreement with that of standard triclinic birnessite (JCPDS 43-1456). The patterns of the CoB samples are very similar to Bir over the low-angle region (5 – $30^\circ 2\theta$), but show significant differences in the high-angle region (30 – $85^\circ 2\theta$) as the (200), (201), (202), (31-1) and (31-2) reflections of triclinic birnessite at 35.7° , 40.1° , 48.7° , 62.9° , and 64.5° (2θ Cu K α), respectively, are weak or absent (Fig. 2a). Cell parameters derived from Rietveld refinement (Fig. S2) show that unit-cell parameter a gradually decreases from 5.171 Å (Bir) to 4.956 Å (CoB20), while other parameters remain stable. As a result, the a/b ratio decreases from 1.818 to 1.736 (Table 2). Taken together, these changes indicate that the layer symmetry of Bir, CoB5 and CoB10 is orthogonal ($a/b > \sqrt{3}$), while the

297 layer symmetry of CoB15 and CoB20 is hexagonal ($a/b \approx \sqrt{3}$), as reported in Yin et al.
298 (2015). The orthogonal layer symmetry in Bir is associated with the substitution of
299 Mn(III) (0.58 Å, low spin) for Mn(IV) (0.53 Å) (Manceau et al., 1997), and the
300 systematic elongation of Jahn–Teller distorted Mn(III) octahedra parallel to the a^*
301 axis (Gaillot et al., 2007). Here, hexagonal symmetry is likely caused by the
302 replacement of Mn(III) by Co(III) in the layer, where the ionic radius of Co(III) (0.54
303 Å, low spin) is sufficiently similar to that of Mn(III) to allow isomorphic substitution
304 (Yin et al., 2015). With an increase in Co content however, the peaks of the CoB
305 samples shift to higher angles, compared to Bir, and this is enhanced in the high-angle
306 region (Fig. 3a). This shift in the XRD peaks occurs because Co(III) has a smaller
307 ionic radius compared to Mn(III).

308 The XRD pattern of Tod (Fig. 2b) is typical of todorokite with characteristic peaks
309 at 2.21 Å (21-2), 1.95 Å (21-3), 1.73 Å (313) and 1.52 Å (21-5) (JCPDS 38-475).
310 Natural todorokite can also display distinct peaks at ~ 7.0 Å ($12-14^\circ 2\theta$) and ~ 4.3 Å
311 ($19-21.5^\circ 2\theta$) (Post et al., 2003; Bodeř et al., 2007; Manceau et al., 2007). These
312 reflections include (10-1) (12.5°) and (101) (13.5°), and (20-1) (19.8°), (10-2) (20.1°),
313 (201) (21.0°) and (102) (21.3°) (JCPDS 38-475). As shown in Figure 4, these
314 reflections are parallel to the b^* axis and connect the corner site of the todorokite
315 structure with the center of the non-adjacent wall, or the diagonal corner site. As such,
316 the geometry of these crystal planes can be used to represent the periodicity of ideal
317 3×3 todorokite tunnel size. The Tod XRD pattern exhibits a broad hump at ~ 7 Å and a
318 shoulder at ~ 4.3 Å rather than distinct peaks, and Tod might therefore possess
319 non-ideal $3 \times n$ tunnel structure. The patterns of the CoT samples are very similar to
320 that of Tod, but the broad hump at ~ 7 Å is very weak, and the shoulder at ~ 4.3 Å is
321 weak or absent (Fig. 3b). The CoT samples might therefore exhibit fewer ideal 3×3
322 tunnels and more non-ideal $3 \times n$ tunnels compared to Tod. Furthermore, in the CoT
323 samples, the 2.39 Å peak is prominent and the 2.46 Å peak, whose intensity increases
324 with increasing Co content, appears as a splitting of the 2.39 Å peak (Fig. 2b). This

325 suggests that the reflux products contain a mixture of ~ 9.6 Å layered structures and
326 todorokite-like tunnel structures (Atkins et al., 2014). With an increase in Co content,
327 the high-angle peaks of the CoT samples shift to higher angles compared to Tod (Fig.
328 2b), while the low-angle peaks shift to lower angles and sharpen (Fig. 3c), consistent
329 with previous reports (Song et al., 2010). These contrasting changes relative to Tod in
330 the high- and low-angle regions of the CoT XRD patterns indicate that Co
331 incorporation causes a shrinkage of the $[\text{MnO}_6]$ octahedral sheets, but an expansion of
332 the distances between tunnel walls or ceilings, and/or adjacent phyllosmanganate
333 layers (Grangeon et al., 2010). We do not observe any peaks attributable to other
334 Co-containing phases in the layered precursors or the reflux products.

335

336 3.1.2 Fourier-transform infrared spectroscopy

337 In FTIR spectra of Mn oxides, the broad peak at ~ 761 cm^{-1} is attributed to the
338 presence of an asymmetric Mn–O stretch from the triple chains of the todorokite
339 lattice (Julien et al., 2004). This absorption band is therefore absent in
340 phyllosmanganates and tectomanganates with 1×1 or 2×2 tunnel sizes and is unique
341 to both ideal (3×3) and non-ideal ($3 \times n$, $n > 3$) todorokite (Julien et al., 2004). In
342 agreement with XRD data, FTIR results show that all reflux products contain
343 todorokite-like structures as evidenced by the presence of this peak at ~ 761 cm^{-1} (Fig.
344 5) (Julien et al., 2004; Atkins et al., 2014; Zhao et al., 2015). The intensity of this peak
345 decreases with Co loading, however, suggesting that the proportion of todorokite-like
346 structures in the reflux products decreases with increasing Co content.

347

348 3.1.3 Nitric acid treatment

349 The XRD patterns (Fig. 6a) of the layered precursors after 1 M HNO_3 treatment
350 for 1 week show reflections at ~ 2.33 , 2.04, 1.72 Å and a more notable peak at 2.46 Å
351 compared to the untreated samples, corresponding to the characteristic diffraction
352 peaks of hexagonal birnessite (JCPDS 23-1239) (Lanson et al., 2000). These

353 differences in the XRD patterns between the layered precursors before and after
354 treatment are most likely related to mineralogical changes resulting from metal
355 release into solution and/or the disproportionation of Mn(III) and its subsequent
356 migration from layer to interlayer sites during the acid treatment. The concentrations
357 of Mn, Co and Mg measured in solution during the acid treatment are shown in Figure
358 7 as a fraction of their total content (Me_χ where Me = Mn, Co or Mg). The fraction of
359 Mn released for all the layered precursors and reflux products is low (Fig. 7a, b)
360 indicating that dissolution of the Mn oxide framework during the acid treatment is
361 limited. As the acid treatment progresses, for each layered precursor, Mn_χ (Fig. 7a)
362 is relatively constant and the final dissolved ratio is generally negatively correlated to
363 the Co content in the samples. This negative correlation might be related to the
364 amount of Mn that is sorbed, where, as Co content increases less Mn is sorbed and
365 thus less Mn is readily removed during the acid treatment. This is potentially
366 corroborated by the Mn AOS (Table 4) which show that as Co content increases there
367 is reduced Mn(III) content. In contrast, Co_χ increases systematically with time (Fig.
368 7c), and Co_χ for CoB10, CoB15 and CoB20 are very similar during the entire
369 treatment while Co_χ for CoB5 is markedly increased, compared to CoB10, CoB15 and
370 CoB20. The limited release of Co from the CoB layered precursors suggests that Co is
371 to a large extent structurally incorporated in the octahedral layers, and that the
372 proportion of such incorporated Co increases with increasing Co content.

373 The XRD patterns of Tod and CoT5 (Fig. 6b) after being treated in 1 M HNO_3 for
374 1 week are not significantly different compared to the untreated samples, whereas
375 CoT10, CoT15 and CoT20 show additional peaks at $\sim 7.2 \text{ \AA}$ and $\sim 3.6 \text{ \AA}$, characteristic
376 of birnessite, the intensity of which increases with Co content. For CoT20 the
377 intensity of these two peaks does not change from 0.75 h to 168 h treatment (Fig. 6c).
378 In contrast to the layered precursors, the Mn_χ for the reflux products increases over
379 time (Fig. 7b), reaching an approximate plateau after 1 week, but the final dissolved
380 ratio is also negatively correlated with the concentration of Co in the samples. Akin to

381 the layered precursors, this negative correlation might indicate that as Co content
382 increases less Mn is sorbed and thus less Mn is readily removed during the acid
383 treatment. The Co_χ values for the reflux products (Fig. 7d) are similar to those of the
384 layered precursors in that they systematically increase with time, but again, Co_χ
385 values are low suggesting that Co is largely structurally incorporated in the reflux
386 products. Finally, the fast and complete release of Mg to solution (Fig. 7e) indicates
387 that all Mg is present as exchangeable and/or sorbed cations in the reflux products. As
388 XRD shows the sole presence of ~ 9.6 Å Mn oxides in the untreated reflux products,
389 the additional presence of ~ 7.2 Å layered minerals after acid treatment indicates that
390 at least part of the released Mg was originally located in phylломanganate interlayers,
391 its release leading to the observed shift of the layer-to-layer distance from ~ 9.6 Å to
392 ~ 7.2 Å. Taken together, the release of Mg to solution upon acid treatment and the
393 presence of characteristic reflections of birnessite in acid-treated CoT10, CoT15 and
394 CoT20 indicate that CoT10, CoT15 and CoT20 contain a mixture of both layered and
395 tunnel structures, consistent with XRD and FTIR data.

396

397 **3.2 Morphology of the reflux products**

398 All reflux products consist of platelets and fibers as shown in HRTEM images
399 (Fig. 8). As expected, Tod occurs mostly as fibrous laths aligned with each other at
400 120° to form large aggregates with a network-like morphology (Fig. 8a, b and c).
401 Both fibrous and trilling patterns are characteristic growth morphologies of todorokite
402 and have been reported in both synthetic and natural samples (e.g., Siegel and Turner,
403 1983; Golden et al., 1986; Feng et al., 2004; Bodei et al., 2007; Atkins et al., 2014).
404 Overall the Tod fibers (Fig. 8c) exhibit lattice fringes with fringe widths of ~ 1 nm,
405 which corresponds to 3 $[\text{MnO}_6]$ octahedra, representing the 3×3 tunnel size of ideal
406 todorokite. In the network-like plates (Fig. 8b) however, there are incoherent tunnel
407 intergrowths with dimensions of 3×4 , 3×5 , 3×7 , 3×8 , 3×10 and 3×12 $[\text{MnO}_6]$
408 octahedra, as reported by Feng et al. (1999), indicating that in the trilling intergrowths

409 the tunnel size in the a^* direction is variable. The observation of these non-ideal $3 \times n$
410 tunnel structures is consistent with the XRD for Tod. The images of the Co-containing
411 reflux products are similar to those of Tod, but CoT samples contain fewer fibers (Fig.
412 8i and j) and more plates (Fig. 8d-h). In addition, two kinds of plates, with and
413 without lattice fringes, can be distinguished in the CoT samples. In the plates with
414 lattice fringes there does not appear to be a predominant fringe size. Representative
415 images are shown for CoT5 and CoT20 in Figure 8e, k and l, with fringe widths
416 corresponding to 3, 4, 5, 6, 7, 9, 10, 11, 12 and 13 $[\text{MnO}_6]$ octahedra, corresponding
417 to a wide range of $3 \times n$ ($n \geq 3$) tunnel sizes. The increased abundance of non-ideal $3 \times n$
418 tunnel sizes, compared to Tod, agrees with the XRD for the CoT samples. Plates with
419 smooth surfaces and without visible lattice fringes are observed in CoT20 (Fig. 8j),
420 both features being characteristic of layered structures. The presence of layered
421 structures in the reflux products is consistent with the XRD, FTIR and acid treatment
422 results. Electron diffraction patterns of representative plates for Tod, CoT5, CoT15
423 and CoT20 (Supplementary Information Fig. S3) are all similar, and show
424 pseudo-hexagonal symmetry due to the fringes arranged in three directions (Golden et
425 al., 1986). The presence of Co in these plates is supported by the energy dispersive
426 spectrometry peak at ~ 6900 eV (Co $K\alpha$) (Supplementary Information Fig. S3).

427

428 3.3 Physicochemical analyses of layered precursors and reflux products

429 The elemental composition of the layered precursors and reflux products (Table 4)
430 indicate that as Co content increases in the CoB and CoT samples the Mn content
431 decreases significantly, relative to Bir and Tod, respectively. This is likely due to the
432 substitution of Co for Mn in the crystal structure (Loganathan et al., 1973; Onda et al.,
433 2007), although there is likely some surface adsorption of Co at the edge sites and/or
434 above and below the vacancy sites (Manceau et al., 1997). It is noticeable that the Mn
435 content in the reflux products shows a greater reduction than in the corresponding
436 layered precursors, with no significant modification of the average oxidation state

437 (AOS) of Mn (Table 3). On the other hand, the Co content (wt% and mol%) is
438 approximately equivalent or slightly higher in the reflux products compared to their
439 corresponding layered precursors. This may indicate that during reflux more Mn is
440 lost from the layered precursors relative to Co and that the transformation of the
441 layered precursors into tunnel products favours the structural incorporation of Co.

442 The surface areas of CoT samples are significantly lower than that of Tod (Table
443 4), which might indicate that the todorokite-like product in the CoT samples (or the
444 mixture of the todorokite-like product and layered Mn oxides) has increased particle
445 size compared to Co-free Tod.

446 The conductivity of the reflux solutions measured at the end of the reflux process
447 are 26.4, 23.5, 32.0, 25.6 and 24.8 $\mu\text{S}/\text{cm}$ for Tod, CoT5, CoT10, CoT15 and CoT20,
448 respectively, indicating that the release to solution of Co, Mn and Mg and
449 corresponding OH and residual Cl anions during todorokite formation was limited.
450 The total concentration of dissolved solids derived from the conductivity values
451 (McNeil and Cox, 2000) is ~ 20 mg/L, equating to a dissolution of ~ 8 mg of solid
452 from the initial 5-7 g used in each reflux.

453

454 **3.4 Crystal chemistry of Mn and Co in layered precursors and reflux products**

455 *3.4.1 Mn K-edge XANES*

456 The Combo method (Manceau et al., 2012) is applied to fit the first derivatives of
457 the Mn K-edge XANES spectra to determine the proportions of Mn(II), Mn(III) and
458 Mn(IV), and thus the Mn AOS in the layered precursor and reflux minerals. Results
459 are shown in Table 3 and the Supplementary Information (Fig. S4 and Table S1). The
460 CoB and CoT samples possess more Mn(IV) and less Mn(III) relative to Bir and Tod,
461 respectively, slightly increasing the Mn AOS, consistent with previous reports
462 (Manceau et al., 1997). The decrease in Mn(III) relative to Bir and Tod most likely
463 arises from Co(III) substitution for Mn(III) (Manceau et al., 1997; Song et al., 2010;
464 Simanova and Peña, 2015). The Mn AOS values are not significantly different

465 between the layered precursors and their reflux products, however, consistent with
466 previous work (Atkins et al., 2014).

467

468 3.4.2 Mn K-edge EXAFS

469 In Mn K-edge EXAFS spectra, the region from 6.5~9.5 Å⁻¹ is especially sensitive
470 to the crystal chemistry of Mn in the Mn oxide structure (McKeown and Post., 2001;
471 Manceau et al., 2002, 2004; Gaillot et al., 2003) and as such it is defined as an
472 “indicator” region for Mn oxides (Marcus et al., 2004; Manceau et al., 2004). The
473 frequency, amplitude and shape of the Mn K-edge EXAFS spectra are similar over the
474 entire wavenumber range for all samples, indicating that they possess a common basic
475 structure (Grangeon et al., 2010; Fig. 9a and b). Notably however, the frequencies of
476 the CoB and CoT spectra are right-shifted relative to Bir and Tod spectra, respectively
477 (Fig. 9a and b). In agreement with the Mn AOS results, this is attributed to a decrease
478 in Mn(III) content (Marcus et al., 2004) and the associated reduction of interatomic
479 distances. Furthermore, the amplitude and shape of the spectra for the layered
480 precursors and reflux products evolve as a function of Co content (Fig. 9a and b).
481 Specifically, with increasing Co content the features at 6.8, 8.0, 9.3 and 10.5 Å⁻¹ and
482 the troughs at 7.3, 9.8 and 11.2 Å⁻¹ increase in amplitude and become sharper. In
483 particular, for Bir, the features at ~8 and ~9 Å⁻¹ have relatively low amplitude and are
484 split, as expected for triclinic birnessite, reflecting the pseudo-orthogonal layer
485 symmetry in its sheets (Manceau et al., 2004; Webb et al., 2005; Gaillot et al., 2007).
486 With increasing Co content, these features increase in amplitude and become single
487 peaks, as expected for hexagonal birnessite, and consistent with a lower content of
488 Jahn-Teller distorted octahedra in the layer structure (Manceau et al., 2004; Marcus et
489 al., 2004; Gaillot et al., 2007). As such, both the XRD and Mn K-edge EXAFS
490 indicate that the layered precursors evolve from triclinic birnessite (Bir) to hexagonal
491 birnessite (CoB15, CoB20) with increasing Co content. For Tod, the features at ~8
492 and ~9 Å⁻¹ have relatively low amplitude and the feature at ~9 Å⁻¹ is broad with a

493 pronounced shoulder on the low wavenumber side, consistent with todorokite spectra
494 (Webb et al., 2005; Feng et al., 2010; Atkins et al., 2014). With increasing Co content
495 these features increase in amplitude and the feature at $\sim 9 \text{ \AA}^{-1}$ becomes much sharper
496 with a loss of the shoulder shape, resembling more closely the shape expected for
497 layered Mn oxides (McKeown and Post, 2001; Webb et al., 2005). As such, the XRD,
498 FTIR, acid treatment, HRTEM and Mn K-edge EXAFS all indicate that the reflux
499 products contain a mixture of layered and tunnel Mn oxides.

500 Concomitant changes are evident in the Fourier transforms of the CoB and CoT
501 spectra, relative to the Bir and Tod spectra, respectively (Fig. 9c and d). The three
502 peaks at ~ 1.5 , ~ 2.5 and $\sim 3 \text{ \AA}$ ($R+\Delta R$) are common to layered and tunnel structure Mn
503 oxides and correspond to the first Mn-O, first Mn-Me edge-sharing (Mn-Me_E) and
504 second Mn-Me corner-sharing (Mn-Me_C) shell distances, respectively (e.g., Manceau
505 et al., 1988, 2007; Silvester et al., 1997; Gaillot et al., 2003; Marcus et al., 2004;
506 Peacock and Sherman, 2007b; Peña et al., 2010). The Mn-Me_E distance reflects the
507 interatomic distance between adjacent edge-sharing Mn-Mn octahedra, present in the
508 layers of layered Mn oxides, and in the walls and ceilings of tunnel Mn oxides (Fig. 1).
509 The Mn-Me_C distance reflects the interatomic distance between adjacent
510 corner-sharing Mn-Mn octahedra, which can be present in both layered and tunnel Mn
511 oxides when cations adsorb above/below vacant layer sites and/or at edge sites
512 (Manceau et al., 2007), but are largely present in tunnel Mn oxides due to the
513 configuration of the Mn₂ / Mn₄ sites (Fig. 1) (Kim et al., 2003; Webb et al., 2005).
514 Notably, the reflux products show a more defined and thus easily identifiable peak at
515 $\sim 3 \text{ \AA}$ ($R+\Delta R$) compared to their corresponding layered precursor, but the definition of
516 this feature weakens with increasing Co content. This suggests that the reflux
517 products contain more corner-sharing linkages than their layered precursors, but that
518 the proportion of these linkages, and thus the proportion of todorokite-like structures
519 in the reflux products, decreases with increasing Co content, consistent with FTIR
520 results.

521 To interpret the Mn K-edge EXAFS more quantitatively, the spectra were fit using
522 a procedure similar to that of Grangeon et al. (2010). Fit parameters are shown in
523 Table 5 and the Supplementary Information (Fig. S5). The fitting results show that the
524 Mn-Me_E bond distances of the layered precursors and reflux products steadily
525 decrease with increasing Co content (Table 5 and Fig. 10). This is likely caused by the
526 substitution of smaller Co(III) for Mn(III), as also evidenced by the shift towards
527 lower *d*-values of the high-angle XRD peaks for the CoB and CoT samples (Fig. 2).
528 Results also show that the ratio of Mn-Me_C to Mn-Me_E (CN_C/CN_E) increases from the
529 CoB to CoT samples, and decreases slightly from Co-free Tod to Co-containing
530 CoT20, confirming that the reflux products contain more corner-sharing linkages than
531 their layered precursors, and supporting the inference that the proportion of
532 corner-sharing linkages in the reflux products, and thus of todorokite-like structures,
533 decreases with increasing Co content (Table 5).

534 The Mn K-edge $\chi(k)$ spectra were also fit as a linear combination of the CoT5 and
535 corresponding CoB spectra, used as reference compounds for tunnel and layered Mn
536 oxides, respectively, to assess the relative proportions of both components in the reflux
537 products (Table 6 and the Supplementary Information, Fig. S6). Fitting indicates that
538 CoT10, CoT15 and CoT20 contain ~80-70% layered ~9.6 Å Mn oxide and ~20-30%
539 tunnel todorokite-like Mn oxide. These values are in good agreement with the
540 proportions of layered and tunnel Mn oxides in natural hydrothermal ferromanganese
541 samples (Atkins et al., 2016). The linear combination fitting results indicate that the
542 proportion of todorokite-like structures in the reflux products decreases with increasing
543 Co content, consistent with the FTIR results and the Mn K-edge EXAFS fitting.

544

545 3.4.3 Co K-edge EXAFS

546 The frequency, amplitude and shape of the Co K-edge EXAFS spectra, in both *k*-
547 and *r*-space, are very similar to one another for both the layered precursors (except for
548 CoB5 which has low Co content and is therefore poor quality) (Fig. 11a) and the

549 reflux products (Fig. 11b). These spectra resemble those collected at the Mn K-edge
550 EXAFS, thus implying that Co possesses a very similar local coordination
551 environment in the layered and reflux samples, and that this environment is similar to
552 that of Mn.

553 To interpret the Co K-edge EXAFS more quantitatively, spectra are fit using a
554 procedure similar to that of Grangeon et al. (2010). Fit parameters are shown in Table
555 7 and the Supplementary Information (Fig. S7). In this fitting approach, a f parameter
556 is used to estimate the relative proportion of Co in Co-Me_E edge-sharing
557 configuration in the CoB and CoT samples (Table 7). Similar to the Mn K-edge
558 spectra, the Co-Me_E edge-sharing peak reflects the interatomic distance between
559 adjacent edge-sharing Co-Me octahedra, and can result from the incorporation of Co
560 into the layers of layered Mn oxides (where Co should be surrounded by 6
561 edge-sharing Mn), and the incorporation of Co into the walls or ceilings of tunnel Mn
562 oxides (where Co at the Mn1 / Mn3 site should be surrounded by 6 edge-sharing Mn,
563 while Co at the Mn2 / Mn4 site should be surrounded by 4 edge-sharing Mn) (Fig. 1).
564 As such the relative proportion of Co in Co-Me_E edge-sharing configuration
565 represents the total proportion of Co that is structurally incorporated in the layered
566 precursors and combined layered and tunnel structure reflux products. The Co-Me_C
567 corner-sharing peak reflects the interatomic distance between corner-sharing Co-Me
568 octahedra, and can result from the surface adsorption of Co at triple corner and/or
569 edge sites on layered and tunnel Mn oxides, and from the incorporation of Co into the
570 walls or ceilings of tunnel Mn oxides (at the Mn2 / Mn4 site where Co should be
571 surrounded by 4 corner-sharing Mn) (Fig. 1). For all samples, data was fit assuming
572 that the coordination number of Co in Co-Me_E edge-sharing configuration is 6. This
573 might lead to an overestimation of Co in Co-Me_E edge-sharing configuration, and thus
574 of Co that is structurally incorporated in the CoT samples, because Co incorporated
575 into tunnel structures might occupy the Mn2 / Mn4 site with a Co-Me_E edge-sharing
576 coordination number of 4 (Song et al., 2010). In this case the Co-Me_E edge-sharing

577 coordination number for the CoT samples would be slightly less than 6, and equate to
578 the weighted average of the proportion of Co at the Mn1 / Mn3 site, surrounded by 6
579 edge-sharing Mn, and Co at the Mn2 / Mn4 site, surrounded by 4 edge-sharing Mn.
580 Despite this limitation, the approach provides a reasonable estimate of the ratio of Co
581 in Co-Me_E edge-sharing configuration and thus the proportion of Co that is
582 structurally incorporated in the layered precursors and the combined layered and
583 tunnel structure reflux products.

584 Fitting results show that Co-Me_E bond distances of the layered precursors and
585 reflux products do not significantly change with increasing Co content (Table 7 and
586 Fig. 10), indicating that Co incorporated into the precursor and reflux products is
587 uniformly distributed in the crystals, being mainly surrounded by Mn(IV). Results
588 also show that the *f* parameter, and thus the proportion of nominally structurally
589 incorporated Co, is almost equivalent for the CoB and CoT samples at ~80% (Table 7).
590 For the CoB samples, the distribution of Co between incorporated (~80%) and surface
591 adsorbed (~20%) species is consistent with previous reports (Manceau et al., 1997;
592 Kwon et al., 2013; Yin et al., 2013, 2015). For the CoT samples, which contain a
593 mixture of layered (~80-70%) and tunnel (~20-30%) structure Mn oxides, the
594 distribution of Co between incorporated (~80%) and surface (~20%) species reflects
595 the average coordination environment. Given the limitations of the fitting approach,
596 the proportion of the total Co incorporated into the CoT samples might be less than
597 ~80%.

598

599

4. DISCUSSION

600 4.1 Effect of Co on the transformation of birnessite to todorokite

601 Layered birnessite precursors with a range of Co contents from 0 to 20
602 Co/(Mn+Co) mol% were subjected to a reflux process designed to simulate the
603 transformation of birnessite into todorokite in natural environments. Of the total Co
604 sorbed in the layered birnessite precursors, ~80% is structurally incorporated and ~20%

605 is surface adsorbed. Mineralogical data derived from XRD, FTIR, and acid treatment,
606 combined with morphological data from HRTEM and molecular level data from Mn
607 K-edge EXAFS indicate that, for the Co-free birnessite precursor, the reflux
608 procedure produces a todorokite-like product with dominant ideal 3×3 tunnel sizes in
609 fibrous laths and non-ideal $3\times n$ ($n\geq 3$) tunnel sizes in trillings. In contrast, for the
610 Co-containing birnessite precursors, the reflux procedure leads to todorokite-like
611 products with a wide range of non-ideal $3\times n$ ($n\geq 3$) tunnel sizes, with no apparent
612 predominant tunnel dimension. Furthermore, for the Co-containing birnessite
613 precursors, the reflux procedure yields Mn oxides with both ~ 9.6 Å layered structure
614 and todorokite-like tunnel structure, in which the proportion of tunnel structures
615 decreases with increasing precursor Co content. These results indicate that the
616 presence of Co in birnessite disrupts its transformation to todorokite.

617 The ability of Co to disrupt the transformation of birnessite into todorokite and
618 produce a non-ideal todorokite-like product is very similar to that of Ni and can be
619 attributed to the fact that both Ni(II) and Co(III) are not Jahn–Teller distorted cations.
620 The presence of Jahn–Teller distorted Mn(III) in the birnessite layers is critical to the
621 transformation of birnessite into todorokite because distortion of the Mn(III)
622 octahedral due to the Jahn-Teller effect results in an elongation and thus weakening of
623 the Mn(III)–O bonds (Bodeř et al., 2007; Cui et al., 2008; Atkins et al., 2014;
624 Grangeon et al., 2014, 2015; Zhao et al., 2015). It is at this structurally weak point
625 that phylломanganate layers are most susceptible to kinking which leads to the
626 formation of the todorokite tunnel walls within the phylломanganate interlayers
627 (Atkins et al., 2014; Grangeon et al. 2014). Isomorphic substitution of Jahn–Teller
628 distorted Mn(III) by Co(III) therefore reduces the likelihood of todorokite formation
629 (Atkins et al., 2014; 2016). It is possible that the isomorphic substitution of Mn(III)
630 by Co(III) results in an uneven distribution of Mn(III) within the layers (Grangeon et
631 al., 2015). This might explain the fact that even the most Co-enriched birnessite
632 precursors are able to form a significant proportion of tunnel structures, but that these

633 tunnel structures have non-ideal tunnel dimensions $3 \times n$ ($n \gg 3$ – CoT15 and CoT20,
634 with n up to 13). It is noteworthy that ideal 3×3 tunnel structures are visible in the
635 fibrous laths of the Co-free todorokite reflux product, whereas non-ideal $3 \times n$ ($n \gg 3$)
636 tunnel structures dominate in trilling intergrowths of the Co-containing
637 todorokite-like reflux products. Other studies have also noted the predominance of
638 ideal 3×3 tunnel dimensions in fibrous todorokite (Golden et al., 1986; Post et al.,
639 2003; Feng et al., 2004; Cui et al., 2009). This suggests that ideal todorokite tends to
640 exhibit a fibrous morphology while non-ideal or a -disordered todorokite prefers to
641 form trilling intergrowths, and that the presence of Co(III), and likely of other
642 structurally incorporated non Jahn-Teller distorted cations, promotes the formation of
643 a network-like platy morphology over a fibrous one.

644 In addition to the ability of Co(III) to disrupt the transformation of birnessite into
645 todorokite, the interlayer species in the precursor layered phase may also be important
646 for transformation. In this work a ~ 9.6 Å layered precursor with interlayer Mg was
647 synthesized, and the acid treatment indicates that the reflux products with layered
648 structures also contain Mg as the interlayer species. In the layered precursors, Mg is
649 likely present in a hydrated form as $\text{Mg}(\text{H}_2\text{O})_6^{2+}$, as for busserite (Shen et al., 1994;
650 Post et al., 2003), but under reflux treatment these species might convert to a Mg
651 (hydr)oxide, leading to an asbolane-like structure with islands of (hydr)oxides in the
652 interlayer (Chukhrov et al., 1982, 1987; Manceau et al., 1987, 1992). Interestingly,
653 although the acid treatment results in the dissolution of Mg and the collapse of the
654 reflux product interlayers from ~ 9.6 to ~ 7.2 Å, it cannot distinguish between
655 $\text{Mg}(\text{H}_2\text{O})_6^{2+}$ and Mg (hydr)oxides as both are expected to dissolve and/or to be
656 exchanged under acidic conditions. XRD patterns of reflux products prepared as in
657 the present study and heat treated at 120 °C for 12 hrs do not show a ~ 7.2 Å peak
658 (Song et al., 2010), however, as would be expected from the dehydration of
659 $\text{Mg}(\text{H}_2\text{O})_6^{2+}$ interlayer species (Chukhrov et al., 1987; Shen et al., 1994). The
660 interlayer Mg species in the layered reflux products is therefore resistant to thermal

661 dehydration and thus most likely resembles a (hydr)oxide-like species, similar to the
662 islands of Co/Ni (hydr)oxides present in the interlayers of asbolane (Chukhrov et al.,
663 1982, 1987; Manceau et al., 1987, 1992). The formation of Mg (hydr)oxides
664 sandwiched between phylломanganate layers should result in a slightly higher
665 d-spacing for the layered reflux product compared to todorokite, and thus might
666 explain the shift to higher d-values of the low-angle 00*l* peaks in the XRD patterns of
667 the reflux products (Fig. 3c). Overall, we suggest that the formation of Mg
668 (hydr)oxides during the reflux procedure results in a mixture of stabilized ~9.6 Å
669 asbolane-like layered structures and non-ideal todorokite-like tunnel structures in the
670 reflux products.

671 The fact that Co(III), and other non Jahn–Teller distorted cations, structurally
672 incorporated into birnessite disrupts the transformation of birnessite into todorokite
673 might help explain the often observed predominance of phylломanganates over
674 tectomanganates in terrestrial and marine environments (e.g., Post, 1999; Marcus et
675 al., 2004; Bodeř et al., 2007; Manceau et al., 2014), and the persistence of
676 phylломanganates in marine ferromanganese nodules and crusts that are many
677 millions of years old (e.g., Burns and Burns, 1977).

678

679 **4.2 Implications for the mobility and fate of Co during the transformation of** 680 **birnessite to todorokite**

681 To date only a limited number of studies have investigated the transformation of
682 Co-containing layered Mn oxides into tunnel Mn oxides and the results indicate that
683 precursor Co might be structurally incorporated into newly formed todorokite, by
684 replacing Mn (Ching et al., 1999; Kumagai et al., 2005; Onda et al., 2007; Song et al.,
685 2010). In particular, Song et al. (2010) hypothesize that Co primarily substitutes for
686 Mn(III) in Co-containing todorokite, and that these Mn(III) are likely located at the
687 edge sites (Mn₂ and Mn₄, Fig. 1) of the ideal 3×3 tunnel structure. As such Co(III)
688 might be primarily incorporated at these edge sites (Ostwald, 1986; Song et al., 2010).

689 The mineralogical, morphological and molecular level data obtained in the present
690 study indicate that Co(III) is structurally incorporated into a mixture of $\sim 9.6 \text{ \AA}$
691 asbolane-like and todorokite-like reflux products. Specifically, the shifts in the XRD
692 patterns observed for the Co-containing reflux products, and the HRTEM images
693 showing an enhanced occurrence of non-ideal $3 \times n$, or *a*-disordered, todorokite with
694 larger *n* (*n* up to 13), compared to Co-free todorokite, are both consistent with the
695 presence of Co(III) isomorphically substituted for Mn(III). It is noteworthy that,
696 eventually, as *n* approaches ∞ these tunnel structures will essentially become
697 layered ones. This evolution is accompanied by an increased occurrence of plate-like
698 network morphologies at the expense of fibrous ones. Consistent with these
699 observations, the Co K-edge EXAFS data shows that Co(III) is predominantly present
700 as a structurally incorporated species ($\sim 80\%$) in the mixed layered and tunnel Mn
701 oxide reflux products. The EXAFS fitting procedure can to some extent differentiate
702 between Co that is structurally incorporated at the Mn1 / Mn3 sites vs. the Mn2 / Mn4
703 sites of the newly formed tunnel structures (Fig. 1) because it provides an estimate of
704 the ratio of Co in Co-Me_E edge-sharing configuration compared to Co in Co-Me_C
705 corner-sharing configuration. The Co-Me_E edge-sharing configuration includes Co
706 incorporated into the layers of layered Mn oxides, effectively in a Mn1 / Mn3 position,
707 and Co incorporated into the walls or ceilings of tunnel Mn oxides, at both the Mn1 /
708 Mn3 site and the Mn2 / Mn4 site. The Co-Me_C corner-sharing configuration includes
709 Co surface adsorbed at triple corner and/or edge sites on layered and tunnel Mn
710 oxides, and Co incorporated into the walls or ceilings of tunnel Mn oxides at the Mn2
711 / Mn4 site. As such if there was a substantially different distribution of Co between
712 the Co-Me_E edge-sharing position in the precursors (i.e., Co incorporated in a Mn1 /
713 Mn3 position) and the Co-Me_E edge-sharing positions in the reflux products
714 (comprising the Mn1 / Mn3 site and the Mn2 / Mn4 site) then the estimate of the ratio
715 of Co in Co-Me_E edge-sharing configuration (i.e., the *f* parameter) should change. The
716 fact that it does not is strong evidence that the Co coordination environment is at least

717 largely similar between the precursors and the reflux products, and thus that the reflux
718 products contain Co structurally incorporated at the Mn1 / Mn3 non-edge sites.
719 Previous reports suggest that Co might be incorporated at the Mn2 / Mn4 edge sites
720 and thus the precise location of structurally incorporated Co(III) in tunnel structure
721 Mn oxides deserves further research.

722 The above evidence for structural incorporation of Co(III) in newly formed
723 asbolane-like and todorokite-like Mn oxides can be combined with the
724 physicochemical analyses to comment on the likely mobility of Co during the
725 transformation process. The EXAFS data analysis shows that, from the Co-containing
726 layered precursors to their corresponding reflux products, the distribution of Co
727 between Co-Me_E edge-sharing and Co-Me_C corner-sharing configuration does not
728 substantially change, and therefore the relative bulk distribution of Co is very similar.
729 Moreover, the majority of the Co is present in Co-Me_E edge-sharing configuration,
730 and is thus structurally incorporated, with only a minor amount of Co present in
731 Co-Me_C corner-sharing configuration, [either structurally incorporated in tunnel
732 structures or surface adsorbed on layered and/or tunnel structures](#). For a given metal,
733 structurally incorporated species are generally less susceptible to mobilisation than
734 surface adsorbed species that can be desorbed due to fluctuations in environmental
735 conditions (pH, ionic strength). The transformation process thus appears to maintain
736 the strong sequestration of Co by Mn oxides. Furthermore, the conductivity
737 measurements performed on the final reflux solutions indicate that the concentrations
738 of ions in solution after the transformation process are low and thus the mass of Co
739 lost to solution is also low.

740 Taken together these results suggest that Co(III) associated with layered birnessite
741 precursors is retained in the solid phase during the transformation of
742 birnessite/buserite to mixed ~9.6 Å asbolane-like and todorokite-like products.
743 Despite the common ability of Ni(II) and Co(III) to disrupt the transformation of
744 birnessite into todorokite, this result is in stark contrast to the mobility of Ni(II)

745 during the transformation, where, with a similar proportion of structurally
746 incorporated to surface adsorbed cation, ~50% of the Ni(II) initially associated with
747 the birnessite precursor is released to solution during the transformation ([Atkins et al.,](#)
748 [2016](#)). The difference in the mobility and fate of Ni(II) and Co(III) during the
749 phyllomanganate-to-tectomanganate transformation may be attributed to the
750 differences in their ionic radii and charge. Considering the ionic radii of Ni(II) (0.68
751 Å) and Co(III) (0.54 Å, low spin) compared to Mn(III) (0.58 Å, low spin), the steric
752 match between Co(III) and Mn(III) is favorable over that between Ni(II) and Mn(III),
753 and has been cited as a key parameter for Co uptake by and structural incorporation in
754 Mn oxides ([Burns, 1976](#); [Manceau et al., 1997](#)). Considering the ionic charge, or
755 electronegativity of Ni(II) and Co(III), Co(III) possesses a higher electronegativity
756 than Ni(II) (1.791 vs. 1.574, respectively) and one that is much closer to that of
757 Mn(III) (1.705, low spin) and Mn(IV) (1.923) ([Yin et al., 2013](#)), and thus its
758 incorporation maintains better charge balance. Density functional theory modelling of
759 Co(III) and Ni(II) uptake by birnessite shows that the energy difference between
760 structural incorporation vs. surface adsorption as a triple corner-sharing complex is
761 much lower for Co(III) compared to Ni(II) (Δ -value is -214 kJ/mol vs. -23 kJ/mol).
762 Incorporation of Co(III) is therefore favoured over Ni(II) and moreover, this
763 incorporation is favoured over surface adsorption ([Kwon et al., 2013](#)).

764 Overall the differences in the ionic properties of Co(III) and Ni(II) mean that,
765 although both Ni(II) and Co(III) are non Jahn–Teller distorted, Co(III) provides a
766 more favourable match to the layered and tunnel structure Mn(III) sites compared to
767 Ni(II), and Co(III) is therefore incorporated in the mixed layered and newly formed
768 tunnel structures. By comparison, ~50% of Ni(II) associated with precursor layer
769 structures is lost to solution during the transformation and the remaining Ni(II) is only
770 surface adsorbed on newly formed todorokite, meaning that it is susceptible to
771 desorption and loss to solution ([Atkins et al., 2016](#)). More generally it is apparent that
772 the mobility and fate of transition metals associated with Mn oxides depends on a

773 number of metal properties, including Jahn–Teller distortion, ionic radius and
774 electronegativity, where metal behaviour is selectively dictated by the structure of the
775 Mn oxide. This means that Mn oxides with distinct structures (i.e. layered or tunnel
776 structures) are likely to play unequal roles in the mobility and fate of transition metals
777 in the environment.

778

779 **5. SUMMARY AND CONCLUSIONS**

780 The present study reports the first detailed investigation of the effect of Co content
781 on the transformation of layered precursor Mn oxide birnessite into tunnel structure
782 Mn oxide products, and documents the mobility and fate of Co during the
783 transformation process. The structural incorporation of Co in layered birnessite
784 precursors leads to an overall reduction of Jahn-Teller distorted Mn(III) octahedra in
785 these precursors, a key factor for their transformation to tunnel structures. As a
786 consequence, the presence of such structural Co(III) disrupts the transformation of
787 birnessite into todorokite, leading to the coexistence of a ~ 9.6 Å asbolane-like
788 phylломanganate and a non-ideal, or α -disordered, todorokite-like tectomanganate.
789 Non-ideal todorokite appears as trilling intergrowths with a wide range of tunnel
790 dimensions that form a network plate-like morphology. Contrary to Ni(II), which also
791 disrupts the transformation of layered to tunnel structures, Co(III) is retained in the
792 solid transformation products, predominantly as structurally incorporated species. The
793 results suggest that Co(III) is likely present in the Mn1 and Mn3 non-edge sites of
794 todorokite, in contrast to previous reports. Overall, the transformation of
795 Co-containing birnessite into todorokite in soils and sediments is unlikely to provide a
796 significant source of Co to soil and sediment porewaters. The present study compared
797 to the results of previous work on the behaviour of other transition metals during the
798 transformation of birnessite to todorokite demonstrates that, overall, metal mobility
799 depends on a specific set of metal properties, the relative importance of these being
800 likely dictated by the structure of the host Mn oxide.

801

802 **Acknowledgements**

803 The authors are grateful to Dr. Pengfei An and Yunpeng Liu at Beijing
804 Synchrotron Radiation Facility (BSRF) for their help in X-ray absorption
805 spectroscopy and XRD data collection and analysis. Zhongkuan Wu also thanks Dr.
806 Yuan Chen at Wuhan University for help with English language. This work is
807 supported by the National Key Research and Development Program of China
808 (No.2016YFD0800403) and the Natural Science Foundations of China (No.
809 41271253 and U1432104). Caroline L. Peacock was supported by the Royal Society
810 (Newton Mobility Grant No. IE151033). The present study benefited also from a Cai
811 Yuanpei program between the Key Laboratory of Arable Land Conservation (Wuhan,
812 China) and ISTerre (Grenoble, France).

813

814

6. REFERENCES

- 815 Atkins A. L., Shaw S. and Peacock C. L. (2014) Nucleation and growth of todorokite
816 from birnessite: implications for tracemetal cycling in marine sediments.
817 *Geochim. Cosmochim. Acta* **144**, 109–125.
- 818 Atkins A. L., Shaw S. and Peacock C. L. (2016) Release of Ni from birnessite during
819 transformation of birnessite to todorokite: Implications for Ni cycling in marine
820 sediments. *Geochim. Cosmochim. Acta.* **189**, 158-183.
- 821 Bodeř S., Manceau A., Geoffroy N., Baronnet A. and Buatier M. (2007) Formation of
822 todorokite from vernadite in Ni-rich hemipelagic sediments. *Geochim.*
823 *Cosmochim. Acta.* **71**, 5698-5716.
- 824 Burns R. G. (1976). The uptake of cobalt into ferromanganese nodules, soils, and
825 synthetic manganese (IV) oxides. *Geochim. Cosmochim. Acta.* **40**(1), 95-102.
- 826 Burns R.G. and Burns V.M. (1975) Mechanism for nucleation and growth of
827 manganese nodules. *Nature*, **255**, 130-131.
- 828 Burns R. G. and Burns V. M. (1977). The mineralogy and crystal chemistry of

829 deep-sea manganese nodules, a polymetallic resource of the twenty-first
830 century. *Phil. Trans. R. Soc. London* **A286**, 283-301.

831 Burns R. G., Burns V. M. and Stockman H. W. (1983). A review of the
832 todorokite-buserite problem; implications to the mineralogy of marine
833 manganese nodules. *Am. Mineral.* **68**, 972-980.

834 Burns R. G., Burns V. M. and Stockman H. W. (1985) The todorokite-buserite
835 problem: further considerations. *Am. Mineral.* **70**, 205-208.

836 Ching S., Krukowska K. S. and Suib S. L. (1999) A new synthetic route to
837 todorokite-type manganese oxides. *Inorg. Chim. Acta.* **294**, 123-132.

838 Chukhrov F. V, Drits V. A. and Gorshkov A. I. (1987) Structural transformations of
839 manganese oxides in oceanic nodules. *Int. Geol. Rev.* **29**, 110-121.

840 Chukhrov F. V., Gorshkov A. I., Vitovskaya I. V., Drits V. A., Sistov A. V. and
841 Rudnitskaya Y. S. (1982) Crystallochemical nature of Co-Ni asbolane. *Int. Geol.*
842 *Rev.* **24**, 598-604.

843 Cui H., Feng X., Tan W., He J. Hu R. and Liu F. (2009) Synthesis of todorokite-type
844 manganese oxide from Cu-buserite by controlling the pH at atmospheric pressure.
845 *Micropor. Mesopor. Mat.* **117**, 41-47.

846 Cui H., Liu F., Feng X., Tan W. and Wang M. (2010) Aging promotes todorokite
847 formation from layered manganese oxide at near-surface conditions. *J. Soil*
848 *Sediment* **10**, 1540-1547.

849 Cui H., Liu X., Tan W., Feng X., Liu F. and Ruan H. D. (2008) Influence of Mn (III)
850 availability on the phase transformation from layered buserite to
851 tunnel-structured todorokite. *Clays Clay Miner.* **56**, 397-403.

852 Davies S. H. R. and Morgan J. J. (1989) Manganese (II) oxidation kinetics on metal
853 oxide surfaces. *J. Colloid Interface Sci.* **129**, 63-77.

854 Drits, V.A., Lanson, B., and Gaillot, A.C. (2007) Birnessite polytype systematics and
855 identification by powder X-ray diffraction. *Am. Mineral.* **92**, 771-788.

856 Drits V. A., Silvester E., Gorshkov A. I. and Manceau A. (1997). Structure of synthetic

857 monoclinic Na-rich birnessite and hexagonal birnessite: I. Results from X-ray
858 diffraction and selected-area electron diffraction. *Am. Mineral.* **82**, 946-961.

859 Dublet G., Juillot F., Brest J., Noel V., Fritsch E., Proux O., Olivi L., Ploquin. and
860 Morin G. (2017). Vertical changes of the Co and Mn speciation along a lateritic
861 regolith developed on peridotites (New Caledonia). *Geochim. Cosmochim.*
862 *Acta.* **217**, 1-15.

863 Feng Q., Kanoh H. and Ooi K. (1999) Manganese oxide porous crystals. *J. Mater.*
864 *Chem.* **9**, 319-333.

865 Feng X., Tan W., Liu F., Wang J. and Ruans H. (2004) Synthesis of todorokite at
866 atmospheric pressure. *Chem. Mater.* **16**, 4330-4336.

867 Feng X., Zhu M., Ginder-Vogel M., Ni C., Parikh S. and Sparks D. (2010) Formation
868 of nano-crystalline todorokite from biogenic Mn oxides. *Geochim. Cosmochim.*
869 *Acta.* **74**, 3232-3245.

870 Fuller C. C. and Harvey J. W. (2000) Reactive uptake of trace metals in the hyporheic
871 zone of a mining-contaminated stream, Pinal Creek, Arizona. *Environ. Sci.*
872 *Technol.* **34**, 1150-1155.

873 Gaillot A. C., Drits V. A., Manceau A. and Lanson B. (2007) Structure of the synthetic
874 K-rich phyllomanganate birnessite obtained by high-temperature decomposition
875 of KMnO_4 : Substructures of K-rich birnessite from 1000 °C
876 experiment. *Micropor. Mesopor. Mat.* **98**, 267-282.

877 Gaillot A. C., Flot D., Drits V. A., Burghammer M., Manceau A. and Lanson B. (2003)
878 Structure of synthetic K-rich birnessites obtained by high-temperature
879 decomposition of KMnO_4 . I. Two-layer polytype from a 800°C experiment.
880 *Chem. Mater.* **15**, 4666-4678.

881 Golden D. C., Chen C. C. and Dixon J. B. (1986) Synthesis of todorokite. *Science*,
882 **231**, 717-719.

883 Grangeon S., Fernandez-Martinez A., Warmont F., Gloter A., Marty N., Poulain A.
884 and Lanson B. (2015) Cryptomelane formation from nanocrystalline vernadite

885 precursor: a high energy X-ray scattering and transmission electron microscopy
886 perspective on reaction mechanisms. *Geochem. Trans.* **16**, 12.

887 Grangeon S., Lanson B. and Lanson M. (2014) Solid-state transformation of
888 nanocrystalline phyllomanganate into tectomanganate: influence of initial layer
889 and interlayer structure. *Acta Crystallogr., Sect. B: Struct.* **70**, 828-838.

890 Grangeon S., Lanson B., Lanson M., and Manceau A. (2008) Crystal structure of
891 Ni-sorbed synthetic vernadite: a powder X-ray diffraction study. *Mineral. Mag.*
892 **72**, 1279-1291.

893 Grangeon S., Lanson B., Miyata N., Tani Y. and Manceau A. (2010) Structure of
894 nanocrystalline phyllomanganates produced by freshwater fungi. *Am. Mineral.*
895 **95**, 1608-1616.

896 Grangeon S., Manceau A., Guilhermet J., Gaillot A.C., Lanson M., and Lanson B.
897 (2012) Zn sorption modifies dynamically the layer and interlayer structure of
898 vernadite. *Geochim. Cosmochim. Acta.* **85**, 302-313

899 Julien C. M., Massot M. and Poinsignon C. (2004) Lattice vibrations of manganese
900 oxides: Part I. Periodic structures. *Spectrochim. Acta. A*, **60**, 689-700.

901 Kim H. S., Pasten P. A., Gaillard J. F. and Stair P. C. (2003) Nanocrystalline
902 todorokite-like manganese oxide produced by bacterial catalysis. *J. Am. Chem.*
903 *Soc.* **125**, 14284-14285.

904 Kumagai N., Komaba S., Abe K. and Yashiro H. (2005) Synthesis of metal-doped
905 todorokite-type MnO₂ and its cathode characteristics for rechargeable lithium
906 batteries. *J. Power Sources* **146**, 310-314.

907 Kwon K. D., Refson K. and Sposito G. (2013). Understanding the trends in transition
908 metal sorption by vacancy sites in birnessite. *Geochim. Cosmochim. Acta.* **101**,
909 222-232.

910 Lanson, B., Drits, V.A., Feng, Q., and Manceau, A. (2002a) Structure of synthetic
911 Na-birnessite: Evidence for a triclinic one-layer unit cell. *Am. Mineral.* **87**,
912 1662-1671.

913 Lanson B., Drits V. A., Gaillot A. C., Silvester E., Plançon, A. and Manceau A.
914 (2002b). Structure of heavy-metal sorbed birnessite: Part 1. Results from X-ray
915 diffraction. *Am. Mineral.* **87**, 1631-1645.

916 Lanson B., Drits V. A., Silvester E. and Manceau A. (2000). Structure of H-exchanged
917 hexagonal birnessite and its mechanism of formation from Na-rich monoclinic
918 buserite at low pH. *Am. Mineral.* **85**, 826-838.

919 Llorca, S. (1987) Nouvelles données sur la composition et la structure des
920 lithiophorites d'après de échantillons de Nouvelle-Calédonie. *C. R. Acad. Sci*
921 *Paris - Série II* **304**, 15-18.

922 Llorca, S. (1988) Nouvelles données sur la composition et la structure des asbolanes
923 (Nouvelle-Calédonie). *C. R. Acad. Sci Paris - Série II* **307**, 155-161.

924 Loganathan P. and Bureau R. G. (1973) Sorption of heavy metal ions by a hydrous
925 manganese oxide. *Geochim. Cosmochim. Acta.* **37**, 1277-1293.

926 Manceau A., Drits V. A., Silvester E., Bartoli C. and Lanson B. (1997) Structural
927 mechanism of Co^{2+} oxidation by the phyllomanganate buserite. *Am. Mineral.* **82**,
928 1150-1175.

929 Manceau, A., Gorshkov, A.I., and Drits, V.A. (1992) Structural Chemistry of Mn, Fe,
930 Co, and Ni in Mn hydrous oxides. II. Information from EXAFS spectroscopy,
931 electron and X-ray diffraction. *Am. Mineral.* **77**, 1144-1157.

932 Manceau A., Kersten M., Marcus M. A., Geoffroy N. and Granina L. (2007) Ba and
933 Ni speciation in a nodule of binary Mn oxide phase composition from Lake
934 Baikal. *Geochim. Cosmochim. Acta* **71**, 1967-1981.

935 Manceau A. Lanson M. and Takahashi Y. (2014). Mineralogy and crystal chemistry of
936 Mn, Fe, Co, Ni and Cu in a deep-sea pacific polymetallic nodule. *Am.*
937 *Mineral.* **99**, 2068-2083.

938 Manceau A., Llorca S. and Calas G. (1987) Crystal chemistry of cobalt and nickel in
939 lithiophorite and asbolane from New Caledonia. *Geochim. Cosmochim. Acta.* **51**,
940 105-113.

- 941 Manceau A., Marcus M. A. and Grangeon S. (2012) Determination of Mn valence
942 states in mixed-valent manganates by XANES spectroscopy. *Am. Mineral.* **97**,
943 816–827.
- 944 Manceau A., Marcus M. A. and Tamura N. (2002) Quantitative speciation of heavy
945 metals in soils and sediments by synchrotron X-ray techniques. In *Applications*
946 *of Synchrotron Radiation in Low-temperature Geochemistry and Environmental*
947 *Science*, vol. 49 (eds. P.A. Fenter, M.L. Rivers, N.C. Sturchio and S.R. Sutton).
948 Springer, pp. 341–428.
- 949 Manceau A., Tommaseo C., Rihs S., Geoffroy N., Chateigner D., Schlegel M.,
950 Tisserand D., Marcus M. A., Tamura N. and Chen Z. S. (2005) Natural speciation
951 of Mn, Ni and Zn at the micrometer scale in a clayey paddy soil using X-ray
952 fluorescence, absorption, and diffraction. *Geochim. Cosmochim. Acta* **69**,
953 4007–4034.
- 954 Marcus M. A., Manceau A. and Kersten M. (2004) Mn, Fe, Zn and As speciation in a
955 fast-growing ferromanganese marine nodule. *Geochim. Cosmochim. Acta* **68**,
956 3125–3136
- 957 McKeown D. A. and Post J. E. (2001) Characterization of manganese oxide
958 mineralogy in rock varnish and dendrites using X-ray absorption spectroscopy.
959 *Am. Mineral.* **86**, 701-713.
- 960 McNeil V. H. and Cox M. E. (2000) Relationship between conductivity and analysed
961 composition in a large set of natural surface-water samples, Queensland,
962 Australia. *Environ. Geol.* **39**, 1325-1333.
- 963 Murray J. W. (1975) The interaction of cobalt with hydrous manganese
964 dioxide. *Geochim. Cosmochim. Acta* **39**, 635-647.
- 965 Murray J. W., Balistrieri L. S. and Paul B. (1984) The oxidation State of Manganese
966 in Marine Sediments and Ferromanganese Nodules. *Geochim. Cosmochim. Acta*
967 **48**, 1237-1247.
- 968 Murray J. W. and Dillard J. G. (1979) The oxidation of cobalt(II) adsorbed on

969 manganese dioxide. *Geochim. Cosmochim. Acta* **43**, 781–787.

970 Nicolas-Tolentino E., Tian Z. R., Zhou H., Xia G. G. and Suib S. L. (1999) Effects of
971 Cu^{2+} ions on the structure and reactivity of todorokite-and cryptomelane-type
972 manganese oxide Octahedral molecular sieves. *Chem. Mater.* **11**, 1733-1741.

973 Onda A., Hara S., Kakiyoshi K. and Yanagisawa K. (2007) Synthesis of manganese
974 oxide octahedral molecular sieves containing cobalt, nickel, or magnesium, and
975 the catalytic properties for hydration of acrylonitrile. *Appl. Catal. A* **321**, 71-78.

976 Ostwald J. (1984) Two varieties of lithiophorite in some Australian deposits. *Mineral.*
977 *Mag.* **48**, 383-388.

978 Ostwald J. (1986) Some observations on the chemical composition of todorokite.
979 *Mineral. Mag.* **50**, 336-340.

980 Peacock C. L. (2009). Physiochemical controls on the crystal-chemistry of Ni in
981 birnessite: genetic implications for ferromanganese precipitates. *Geochim.*
982 *Cosmochim. Acta* **73**, 3568-3578.

983 Peacock C. L. and Sherman D. M. (2007a) Crystal-chemistry of Ni in marine
984 ferromanganese crusts and nodules. *Am. Mineral.* **92**, 1087-1092.

985 Peacock C. L. and Sherman D. M. (2007b) Sorption of Ni by birnessite: Equilibrium
986 controls on Ni in seawater. *Chem. Geol.* **238**, 94-106.

987 Peña J., Kwon K. D., Refson K., Bargar J. R. and Sposito G. (2010) Mechanisms of
988 nickel sorption by a bacteriogenic birnessite. *Geochim. Cosmochim. Acta* **74**,
989 3076-3089.

990 Post J. E. (1999) Manganese oxide minerals: crystal structures and economic and
991 environmental significance. *Proc. Natl. Acad. Sci. U. S. A.* **96**, 3447 - 3454.

992 Post J. E. and Appleman D. E. (1988) Chalcophanite, $\text{ZnMn}_3\text{O}_7 \cdot 3\text{H}_2\text{O}$: New
993 crystal-structure determinations. *Am. Mineral.* **73**, 1401-1404.

994 Post, J.E. and Appleman, D.E. (1994) Crystal structure refinement of lithiophorite. *Am.*
995 *Mineral.* **79**, 370-374.

996 Post J. E., Heaney P. J. and Hanson J. (2003) Synchrotron X-ray diffraction study of

997 the structure and dehydration behaviour of todorokite. *Am. Mineral.* **88**, 142 –
998 150.

999 Ravel B. and Newville M. (2006) Athena and Artemis: interactive graphical data
1000 analysis using ifeffit. *Phys. Scripta* **115**, 1007-1010.

1001 Remucal C.K. and Ginder-Vogel, M. (2014) A critical review of the reactivity of
1002 manganese oxides with organic contaminants. *Environ. Sci. Proc. Impacts* **16**,
1003 1247-1266.

1004 Saito M. A. and Moffett J. W. (2002) Temporal and spatial variability of cobalt in the
1005 atlantic ocean. *Geochim. Cosmochim. Acta* **66**, 1943-1953.

1006 Saratovsky I., Gurr S. J. and Hayward M. A. (2009). The structure of manganese
1007 oxide formed by the fungus *Acremonium* sp. strain kr21-2. *Geochim. Cosmochim.*
1008 *Acta* **73**, 3291-3300.

1009 Shen X. F., Ding Y. S., Liu J., Cai J., Laubernds K., Zerger R.P., Vasiliev A., Aindow
1010 M. and Suib S.L. (2005) Control of Nanometer - Scale Tunnel Sizes of Porous
1011 Manganese Oxide Octahedral Molecular Sieve Nanomaterials. *Adv. Mater.* **17**,
1012 805-809.

1013 Shen Y. F., Suib S L and O'Young C. L. (1994) Effects of inorganic cation templates
1014 on octahedral molecular sieves of manganese oxide. *J. Am. Chem. Soc.* **116**,
1015 11020-11029.

1016 Siegel M. D. and Turner S. (1983) Crystalline todorokite associated with biogenic
1017 debris in manganese nodules. *Science* **219**,172-4.

1018 Silvester E., Manceau M. and Drits V. A. (1997) Structure of synthetic monoclinic
1019 Na-rich birnessite and hexagonal birnessite: II. Results from chemical studies
1020 and EXAFS spectroscopy. *Am. Mineral.* **82**, 962-978.

1021 Simanova A. A. and Peña J. (2015) Time-resolved investigation of cobalt oxidation by
1022 Mn (III)-rich δ -MnO₂ using quick X-ray absorption spectroscopy. *Environ. Sci.*
1023 *Technol.* **49**, 10867-10876.

1024 Song C., Li R., Liu F., Feng X., Tan W. and Qiu G. (2010) Cobalt-doped todorokites

1025 prepared by refluxing at atmospheric pressure as cathode materials for Li
1026 batteries. *Electrochim. Acta* **55**, 9157-9165.

1027 Taylor R. M. (1968). The association of manganese and cobalt in soils—further
1028 observations. *Eur. J. Soil Sci.* **19**, 77-80.

1029 Taylor R. M., McKenzie R. M., and Norrish K. (1964) The mineralogy and chemistry
1030 of manganese in some Australian soils. *Aust. J. Soil Res.* **2**, 235-248.

1031 Tebo B. M., Bargar J. R., Clement B. G., Dick G. J., Murray K. J., Parker D., Verity
1032 R., and Webb S.M. (2004) Biogenic manganese oxides: Properties and
1033 mechanisms of formation. *Annu. Rev. Earth Pl. Sci.* **32**, 287-328.

1034 Villalobos M., Bargar J., and Sposito G. (2005) Mechanisms of Pb(II) Sorption on a
1035 Biogenic Manganese Oxide. *Environ. Sci. Technol.* **39**, 569-576.

1036 Villalobos M., Lanson B., Manceau A., Toner B., and Sposito G. (2006) Structural
1037 model for the biogenic Mn oxide produced by *Pseudomonas putida*. *Am. Mineral.*
1038 **91**, 489-502.

1039 Vodyanitskii Y. N., Vasilev A. A., Lesovaya S. N., Sataev E. F., and Sivtsov, A. V.
1040 (2004) Formation of manganese oxides in soils. *Eurasian Soil Sci.* **37**, 572-584.

1041 Webb S. M., Tebo B. M. and Bargar J. R. (2005) Structural characterization of
1042 biogenic Mn oxides produced in seawater by the marine *Bacillus* sp. strain SG-1.
1043 *Am. Mineral.* **90**, 1342-1357.

1044 Yin Y. G., Xu W. Q., Shen Y. F., Suib S. L. and O'Young C. L. (1994) Studies of
1045 oxygen species in synthetic todorokite-like manganese oxide octahedral
1046 molecular sieves. *Chem. Mater.* **6**, 1803-1808.

1047 Yin H., Li H., Wang Y., Ginder-Vogel M., Qiu G., Feng X., Zheng L. and Liu F. (2014)
1048 Effects of Co and Ni co-doping on the structure and reactivity of hexagonal
1049 birnessite. *Chem. Geol.* **381**, 10-20.

1050 Yin H., Liu F., Feng X., Hu T., Zheng L., Qiu G., Koopal L. K. and Tan W. F. (2013).
1051 Effects of Fe doping on the structures and properties of hexagonal birnessites –
1052 comparison with Co and Ni doping. *Geochim. Cosmochim. Acta* **117**, 1-15.

- 1053 Yin H., Liu Y., Koopal L. K., Feng X., Chu S., Zhu M. and Liu F. (2015) High
1054 Co-doping promotes the transition of birnessite layer symmetry from orthogonal
1055 to hexagonal. *Chem. Geol.* **410**, 12-20.
- 1056 Yu Q., Sasaki K., Tanaka K., Ohnuki T. and Hirajima, T. (2012) Structural factors of
1057 biogenic birnessite produced by fungus *Paraconiothyrium*, sp. wl-2 strain
1058 affecting sorption of Co²⁺. *Chem. Geol.* **310–311**, 106-113.
- 1059 Zhao H., Liang X., Yin H., Liu F., Tan W., Qiu G. and Feng X. (2015) Formation of
1060 todorokite from “c-disordered” H⁺-birnessites: the roles of average manganese
1061 oxidation state and interlayer cations. *Geochem. Trans.* **16**, 1-11.

Table 1

Co wt. % and Co mole ratio in layered precursors and reflux products

Samples	Co wt. %	Co/(Mn+Co) mol %
Bir	--	--
CoB5	1.97(2)	3.3
CoB10	4.70(5)	7.7
CoB15	7.55(4)	12.5
CoB20	9.84(7)	16.9
Tod	--	--
CoT5	2.05(4)	3.8
CoT10	4.46(6)	8.3
CoT15	6.81(8)	13.5
CoT20	9.26(12)	17.9

Table 2

Lattice parameters derived from Rietveld refinements* for layered precursors

Samples	a/Å	b/Å	c/Å	$\beta/^\circ$	Rwp/%	a/b
Bir	5.1710(7)	2.8447(4)	7.3309(9)	103.37(2)	6.94	1.818
CoB5	5.1212(16)	2.8491(6)	7.3159(11)	102.65(3)	7.96	1.798
CoB10	5.0134(15)	2.8564(10)	7.2878(18)	101.95(6)	6.08	1.755
CoB15	4.9649(20)	2.8638(10)	7.2876(13)	102.07(4)	6.85	1.734
CoB20	4.9562(14)	2.8553(8)	7.2888(13)	102.30(4)	7.23	1.736

Note: Birnessite initial structural parameters were adapted from JCPDS 43-1456, and during the refinement process, cell parameters and site occupancy in the MnO_6 layer were refined. Co ions in CoB samples were assumed to substitute for Mn sites in the structure, such that the sum of occupation for Mn and Co was fixed to 1.

Table 3

Fractional and average valence states of Mn obtained from a Combo fit of Mn K-edge XANES 1st derivative spectra of layered precursors and reflux products. The estimated error for Combo method is $\pm 4\%$ (Manceau et al., 2012; Yin et al., 2015)

Sample	Mn ²⁺ at. %	Mn ³⁺ at. %	Mn ⁴⁺ at. %	Mn-AOS
Bir	2	26	72	3.69
CoB5	3	17	81	3.78
CoB10	4	27	69	3.64
CoB15	5	7	88	3.83
CoB20	5	9	86	3.80
Tod	2	25	74	3.72
CoT5	2	23	75	3.73
CoT10	4	26	70	3.66
CoT15	2	16	82	3.81
CoT20	5	8	87	3.82

Note: The references used to fit Mn K-edge XANES data are those used by Manceau et al. (2012).

Table 4

Physicochemical properties of layered precursors and reflux products

Samples	Mn wt. %	Mg wt. %	Mg/Mn mol%	Mg/(Mn+Co) mol%	SSA (m ² /g)
Bir	55.4(1.0)	--	--	--	--
CoB5	54.0(2.0)	--	--	--	--
CoB10	52.3(2.3)	--	--	--	--
CoB15	49.2(7)	--	--	--	--
CoB20	45.0(1.8)	--	--	--	--
Tod	54.4(2.1)	3.95(8)	16.4	16.4	90.7
CoT5	48.0(1.2)	3.86(9)	18.2	16.9	47.6
CoT10	46.0(1.5)	3.67(12)	18.1	17.5	86.2
CoT15	40.9(1.2)	3.72(2)	20.6	16.6	51.1
CoT20	39.6(7)	3.58(7)	20.4	17.0	55.0

Note: Na was not detected in samples prepared by Song et al. (2010) with the same method and thus not measured in the present samples.

Table 5

Structural parameters derived from Mn K-edge EXAFS fitting over 1-4 Å

Atomic pairs		Bir	CoB5	CoB10	CoB15	CoB20	Tod	CoT5	CoT10	CoT15	CoT20
Mn-O _{1st}	CN	5.36(89)	5.04(59)	4.30(51)	5.35(64)	5.15(62)	5.46(66)	5.57(69)	4.97(51)	5.51(1.05)	5.44(72)
	R (Å)	1.907(7)	1.908(5)	1.909(5)	1.904(5)	1.906(5)	1.901(6)	1.901(5)	1.903(4)	1.904(8)	1.903(5)
	σ^2 (Å ²)	0.004(1)	0.003(1)	0.003(1)	0.004(1)	0.004(1)	0.004(1)	0.004(1)	0.004(1)	0.003(1)	0.004(1)
Mn-O _{2nd}	R (Å) ^{a)}	3.610(81)	3.656(31)	3.641(33)	3.644(31)	3.635(30)	3.582(57)	3.601(40)	3.625(29)	3.636(78)	3.623(34)
Mn-Me _E	CN	5.91(1.54)	6.19(75)	5.00(67)	6.12(68)	5.58(68)	4.63(90)	5.22(76)	4.99(59)	5.49(93)	5.53(75)
	R (Å)	2.901(10)	2.895(6)	2.884(6)	2.874(6)	2.871(7)	2.883(7)	2.874(6)	2.874(6)	2.866(8)	2.864(6)
	σ^2 (Å ²)	0.008(2)	0.007(1)	0.005(1)	0.006(1)	0.005(1)	0.006(1)	0.006(1)	0.006(1)	0.006(1)	0.005(1)
Mn-Me _C	CN	2.61(1.32)	2.76(71)	2.14(55)	2.69(65)	2.52(54)	2.60(83)	2.97(70)	2.75(58)	2.99(88)	2.86(76)
	R (Å)	3.466(72)	3.512(23)	3.501(24)	3.500(20)	3.496(18)	3.450(38)	3.463(23)	3.483(18)	3.485(37)	3.477(18)
CN _C /CN _E		0.44	0.45	0.43	0.44	0.45	0.56	0.57	0.55	0.54	0.52
δE_0 (eV)		-7.12(1.63)	-6.56(1.04)	-5.49(98)	-8.17(1.12)	-7.38(98)	-7.15(1.33)	-8.12(1.07)	-5.35(95)	-7.98(1.66)	-8.14(1.05)
R factor (%)		0.04	0.01	0.01	0.01	0.01	0.02	0.02	0.01	0.01	0.01

Coordination numbers (CN) and Debye-Waller factors (σ^2) of Mn-O shells were refined together, as were Debye-Waller factors of the two Mn-Me shells.

Table 6

Best fits via linear combination fitting of Mn K-edge $\chi(k)$ for reflux products

Sample	Best Fitting	Error
CoT10	0.33 CoT5 + 0.67 CoB10	0.09
CoT15	0.23 CoT5 + 0.77 CoB15	0.07
CoT20	0.21 CoT5 + 0.79 CoB20	0.04

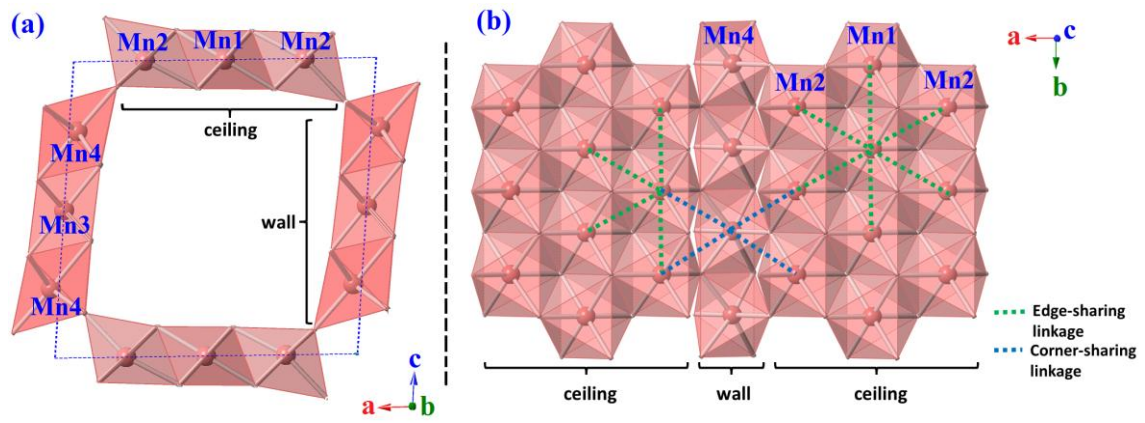
Table 7

Structural parameters derived from Co K-edge EXAFS fitting over 1-4 Å

Atomic pairs		CoB5	CoB10	CoB15	CoB20	CoT5	CoT10	CoT15	CoT20
Co-O1st	CN	6.62(1.58)	4.66(66)	5.75(88)	4.61(51)	7.21(2.62)	5.21(66)	4.91(59)	4.77(69)
	R (Å)	1.909(9)	1.913(5)	1.909(8)	1.915(5)	1.907(17)	1.913(6)	1.913(5)	1.914(7)
	$\sigma^2(\text{Å}^2)$	0.001(1)	0.001(1)	0.004(1)	0.002(1)	0.004(2)	0.002(1)	0.002(1)	0.002(1)
Co-O2nd	R(Å)a	3.713(52)	3.460(46)	3.660(29)	3.495(35)	3.666(34)	3.469(45)	3.486(37)	3.481(44)
Co-MeE	CN	6*f	6*f	6*f	6*f	6*f	6*f	6*f	6*f
	R (Å)	2.836(14)	2.849(5)	2.843(6)	2.851(5)	2.840(13)	2.850(5)	2.848(5)	2.846(6)
	$\sigma^2(\text{Å}^2)$	0.002(1)	0.003(1)	0.002(0.5)	0.003(0.5)	0.002(1)	0.003(1)	0.003(1)	0.003(1)
Co-MeC	CN	6*(1-f)	6*(1-f)	6*(1-f)	6*(1-f)	6*(1-f)	6*(1-f)	6*(1-f)	6*(1-f)
	R (Å)	3.528(68)	3.364(57)	3.474(16)	3.401(35)	3.475(34)	3.469(37)	3.395(29)	3.404(30)
f		0.84(13)	0.86(9)	0.75(5)	0.77(6)	0.73(14)	0.83(10)	0.79(7)	0.81(10)
$\delta E0$ (eV)		-3.75(2.50)	-0.81(91)	-2.09(1.32)	-0.37(94)	-3.13(2.62)	0.12(1.03)	-0.51(99)	-0.05(1.07)
R factor (%)		0.04	0.003	0.006	0.003	0.05	0.005	0.004	0.006

Coordination numbers (CN) and Debye-Waller factors (σ^2) of Co-O shells were refined together, as were Debye-Waller factors of the two Co-Me shells.

Parameter f represents the proportion of Co in an edge-sharing configuration in each of the CoB and CoT sample.



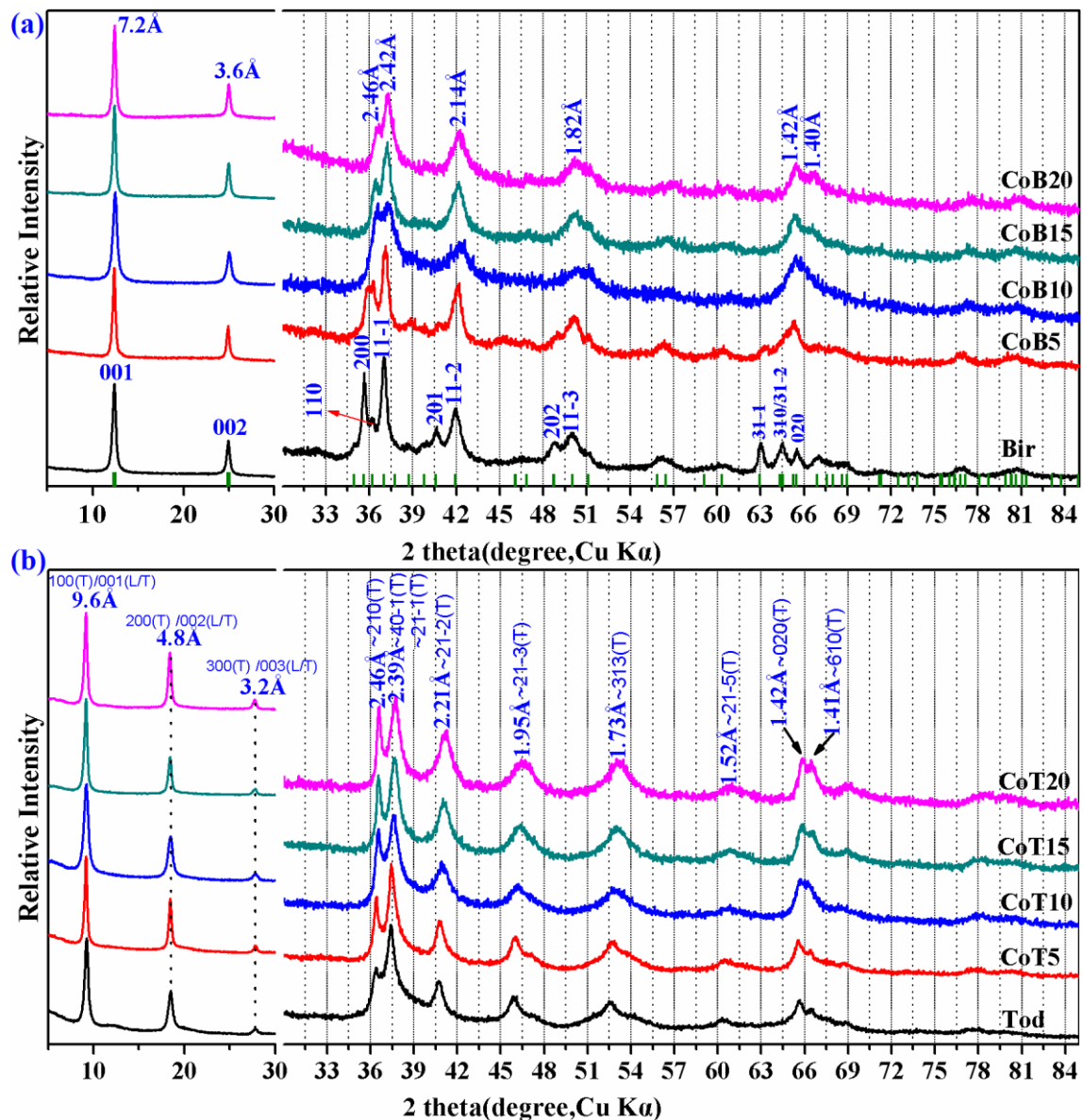
1

2 Fig. 1 Crystal structure of todorokite with a 3x3 tunnel size observed along b^* (a) and c^* (b)

3 direction

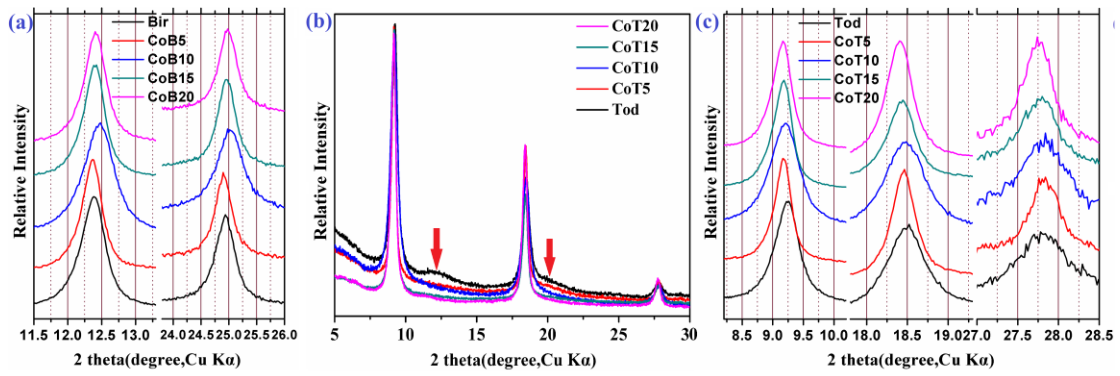
4

5



6
7
8
9
10
11

Fig. 2. Powder XRD patterns of layered precursors (a) and reflux products (b). Diffracted intensities peaks are normalized in the low and high angle region. Green ticks at the bottom of (a) indicate reflections of triclinic birnessite (JCPDS 43-1456). In (b), (L) and (T) indicate reflections of 9.6 Å layered Mn oxide and of todorokite (JCPDS 38-475), respectively.

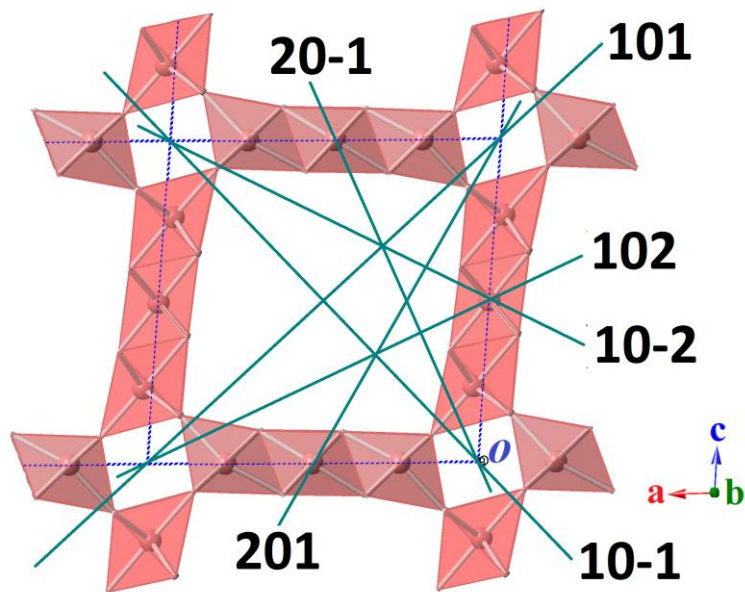


12

13 Fig. 3. Powder XRD patterns in the low angle region of the layered precursors (a), and the reflux
 14 products (b) and (c). Arrows in (b) indicate the broad hump and shoulder in the patterns.

15

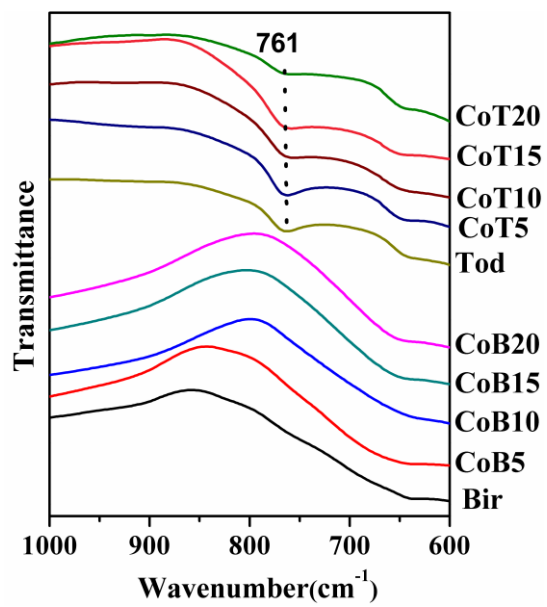
16



17

18 Fig. 4. Lattice planes of todorokite with a uniform 3×3 tunnel structure

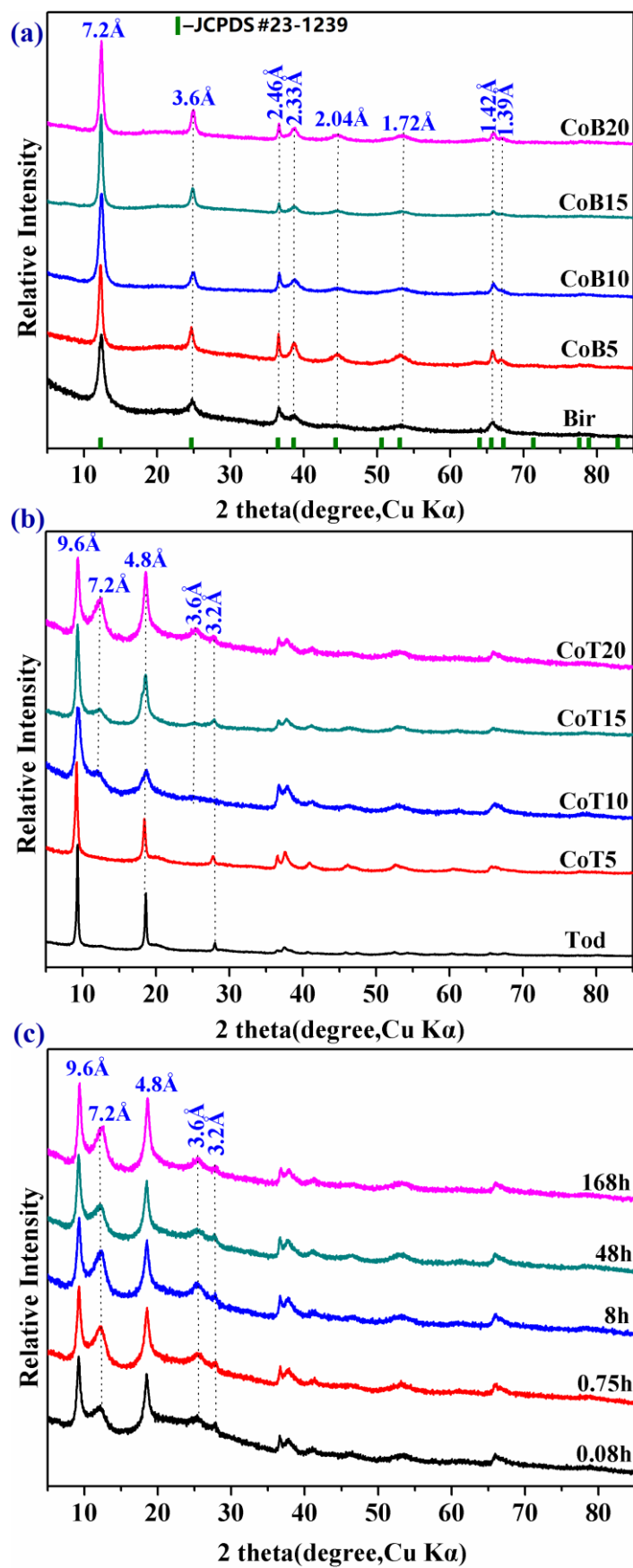
19



20

21 Fig. 5. FTIR spectra of layered precursors (bottom) and reflux products (top)

22

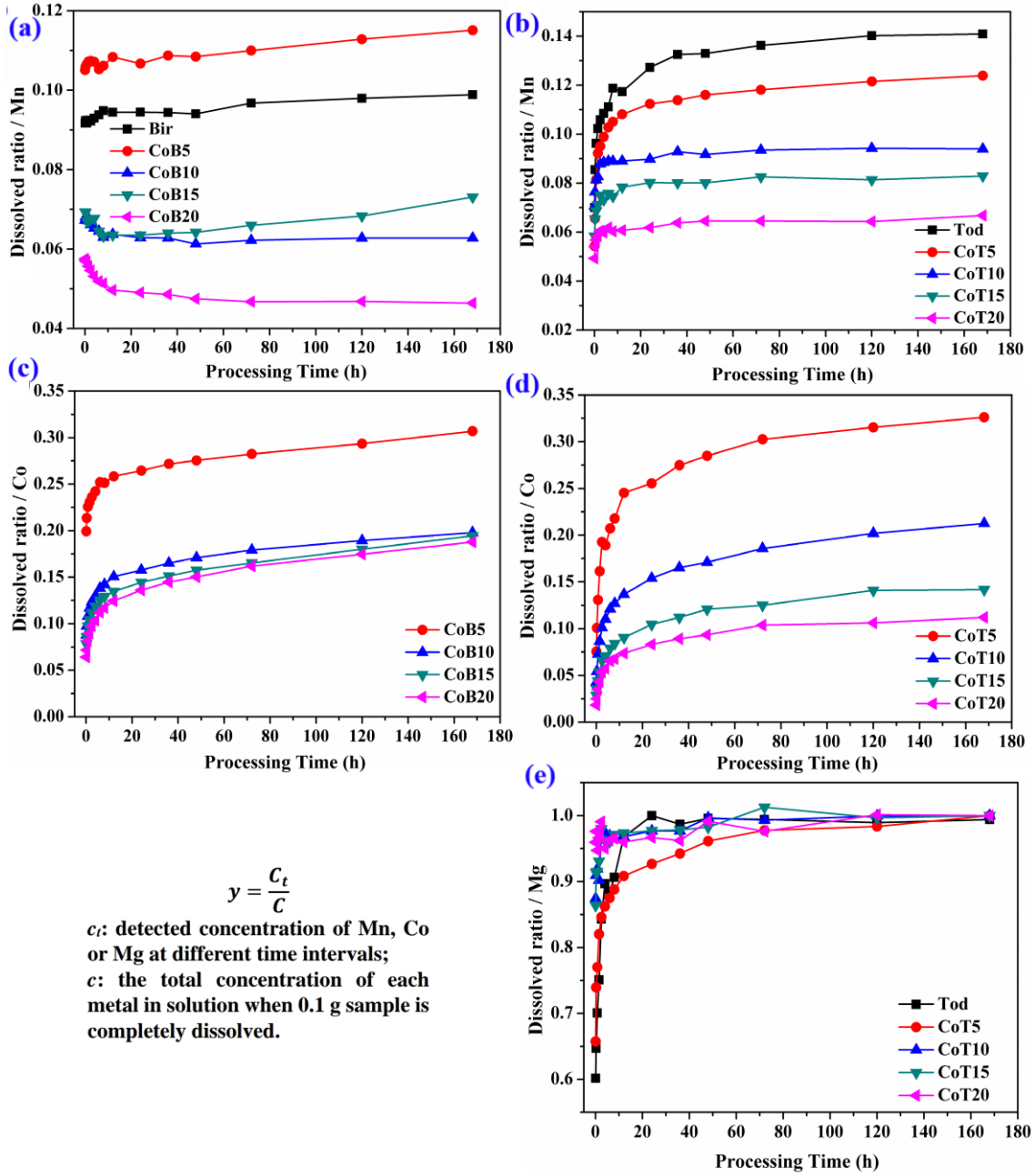


23

24 Fig. 6. XRD patterns of layered precursors and reflux products after nitric acid treatment: (a) layered

25 precursors; (b) reflux products; (c) sample CoT20 after different nitric acid treatment durations.

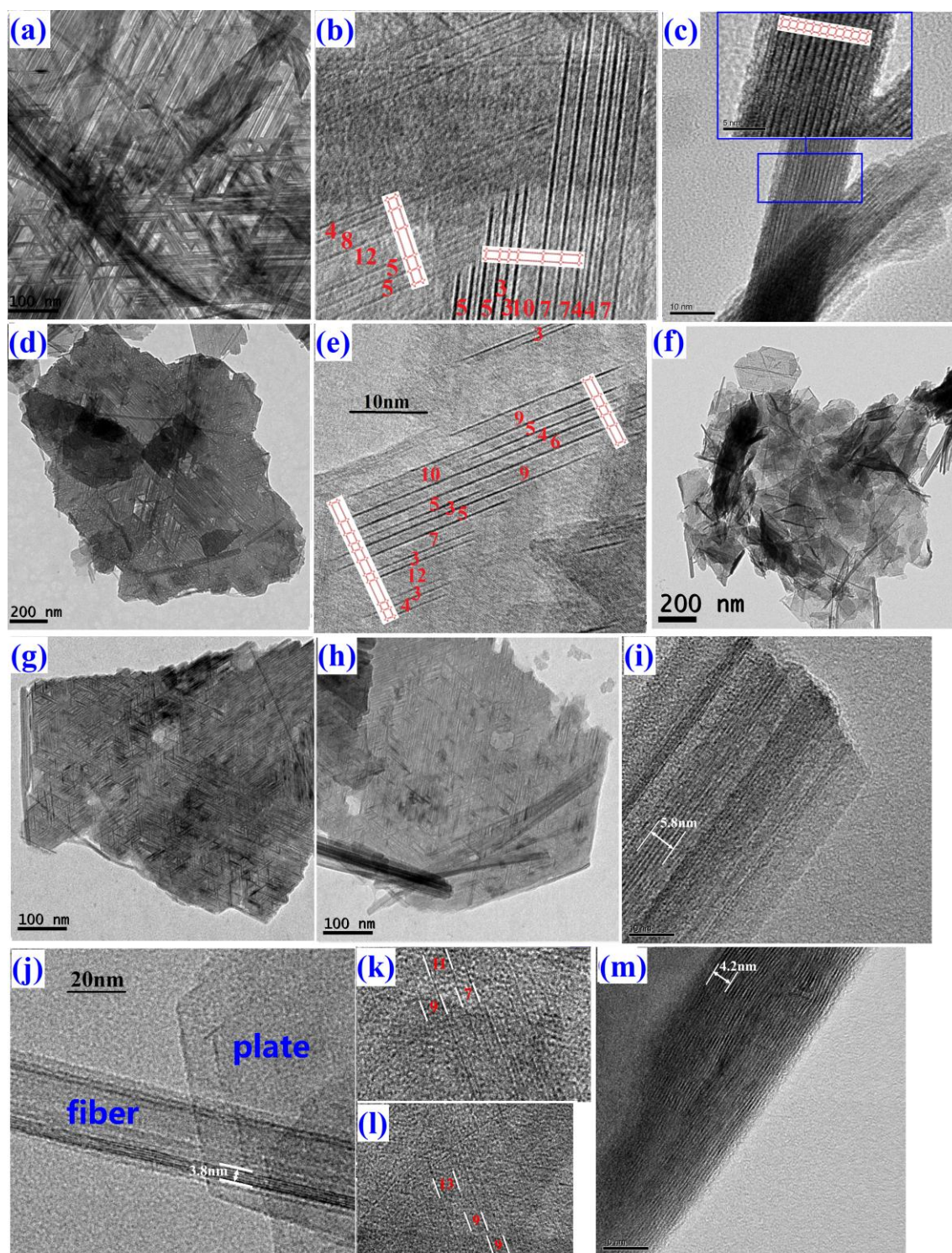
26



27

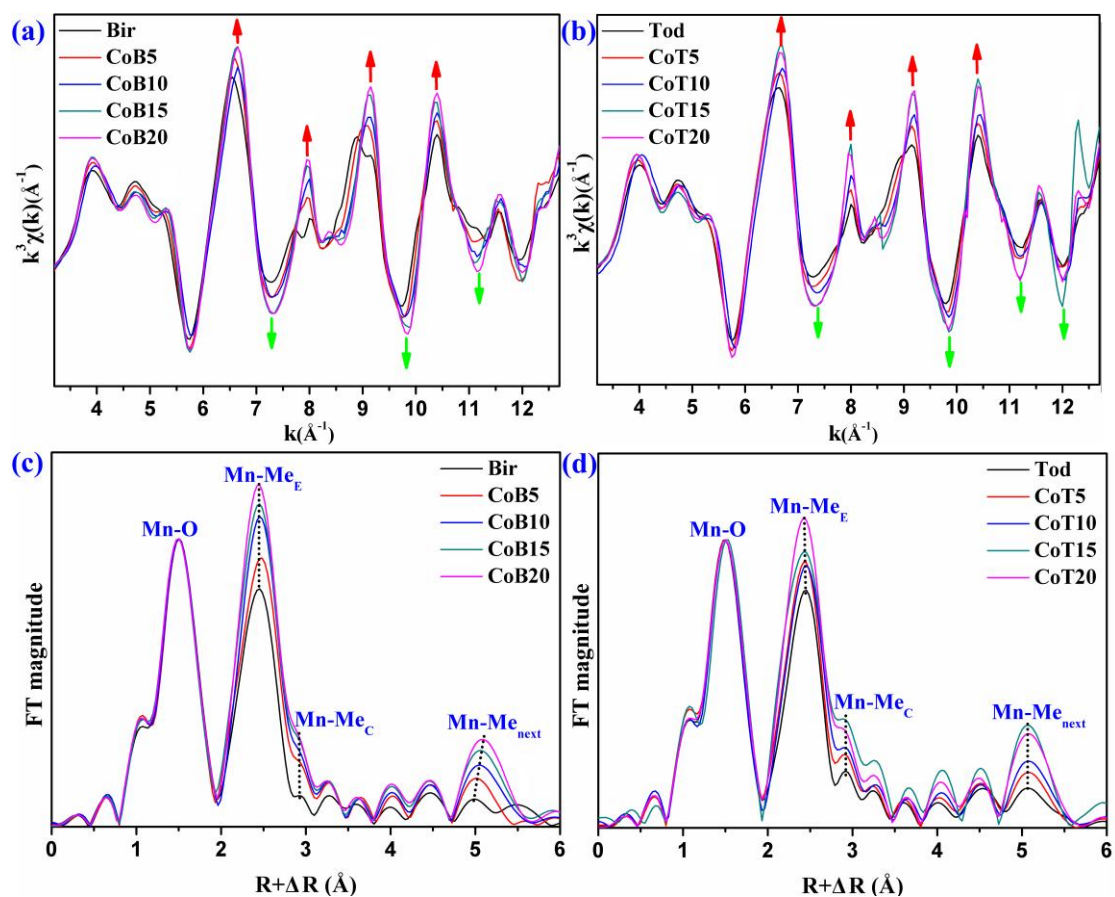
28 Fig. 7. Ratios of element (Mn, Co, Mg) released during nitric acid treatment. Mn for CoB (a) and

29 CoT (b). Co for CoB (c) and CoT (d). Mg for CoT (e).



30

31 Fig. 8. High resolution transmission electron microscopy images: Tod: (a-c); CoT5: (d and e);
 32 CoT10: (f); CoT15: (g); CoT20: (h-m). Red numbers in the pictures indicate the number of MnO₆
 33 octahedra between lattice fringes, models schematize the structure of marked areas observed along
 34 the b^* direction. White labels in (i), (j) and (m) indicate the distance corresponding to 6, 4 and 6
 35 lattice fringes, respectively.

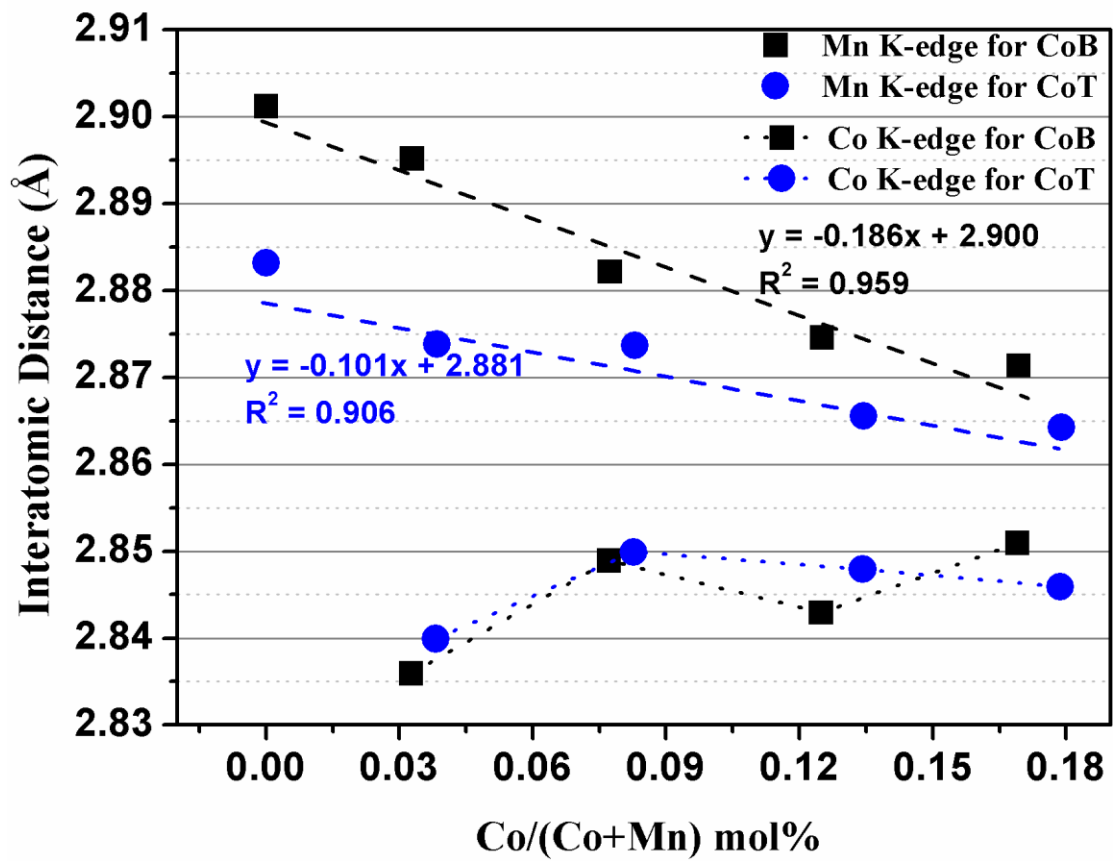


36

37 Fig. 9. Mn K-edge EXAFS spectra (a and b) and their respective Fourier transforms (c and d) for
 38 layered precursors and reflux products. Arrows in (a) and (b) highlight modifications of signal
 39 amplitude (see text for details). Intensity of the Fourier transforms are normalized to the first Mn-O
 40 shell (c and d).

41

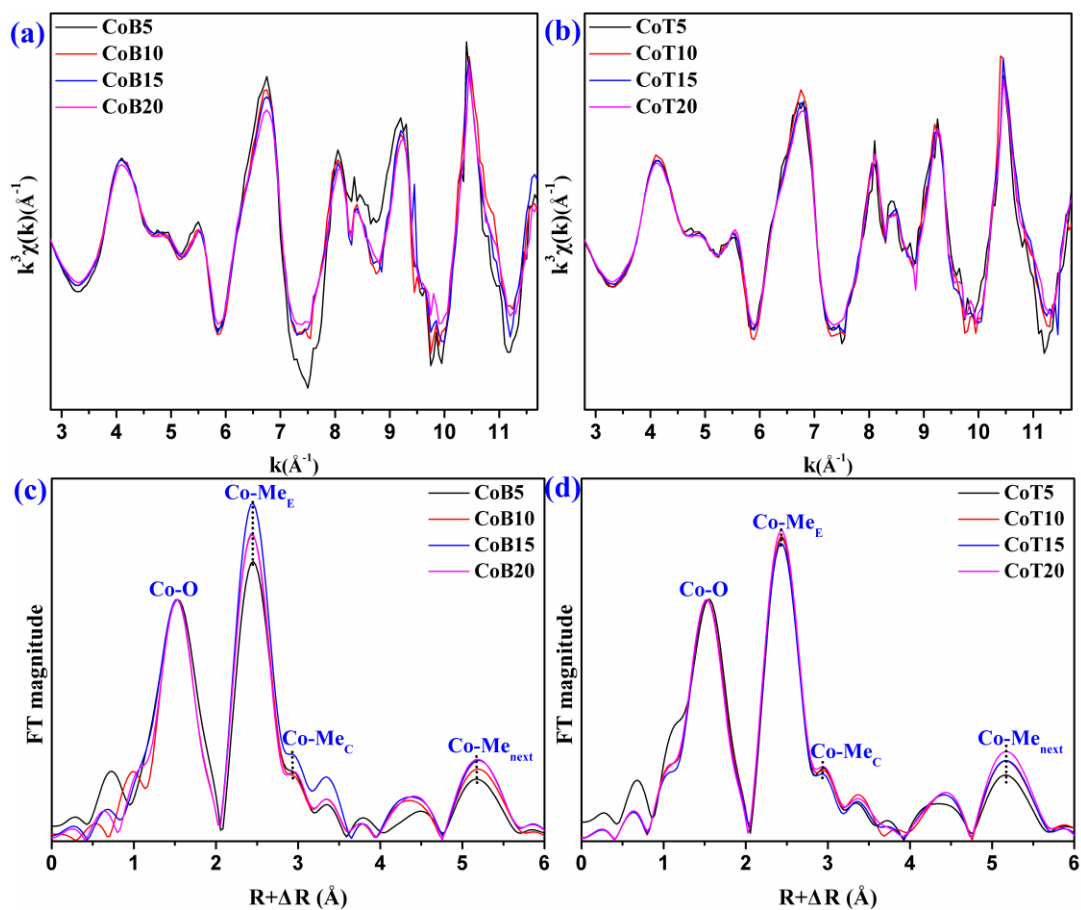
42



43

44 Fig. 10. Evolution of interatomic Mn/Co-Me_E distances in layered precursors and reflux products as
 45 a function of their Co content.

46



47

48 Fig. 11. Co K-edge EXAFS spectra (a and b) and their respective Fourier transforms (c and d) for
 49 layered precursors and reflux products. Intensity of the Fourier transforms are normalized to the first
 50 Mn-O shell (c and d).

51

Supplementary information to:

Transformation of Co-containing birnessite to todorokite: Effects of Co on the transformation and implications for Co mobility

Zhongkuan Wu^a, Caroline L. Peacock^b, Bruno Lanson^c, Hui Yin^a, Lirong Zheng^d, Zhongjun Chen^d, Wenfeng Tan^a, Guohong Qiu^a, Fan Liu^{a,*}, Xionghan Feng^{a,*}

^a*Key Laboratory of Arable Land Conservation (Middle and Lower Reaches of Yangtse River) Ministry of Agriculture, College of Resources and Environment, Huazhong Agricultural University, Wuhan 430070, China.*

^b*School of Earth and Environment, University of Leeds, Leeds LS2 9JT, UK.*

^c*University of Grenoble Alpes, CNRS, ISTERre, F-38000 Grenoble, France.*

^d*Beijing Synchrotron Radiation Facility, Institute of High Energy Physics, Chinese Academy of Sciences, Beijing 100039, China.*

*Corresponding author:

Tel: +86 27 87280271

E-mail: liufan@mail.hzau.edu.cn (F. Liu), fxh73@mail.hzau.edu.cn (X. Feng).

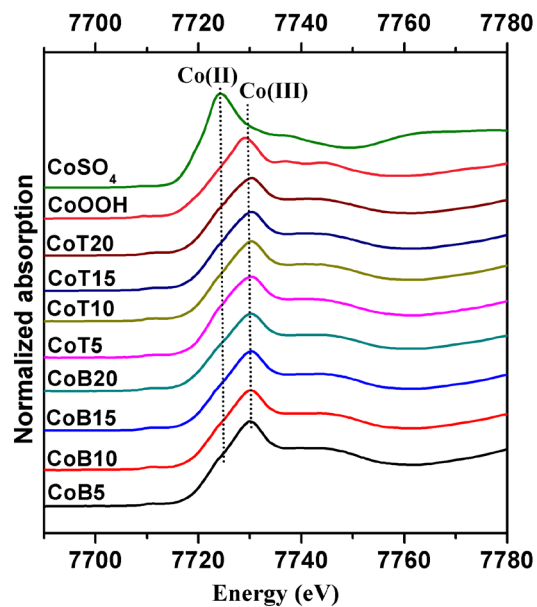


Fig. S1. Co K-edges XANES spectra of Co in CoB, CoT and two standard samples of Co(II) (CoSO₄) and Co(III) (CoOOH), indicating that the oxidation state of Co in CoB and CoT is Co(III).

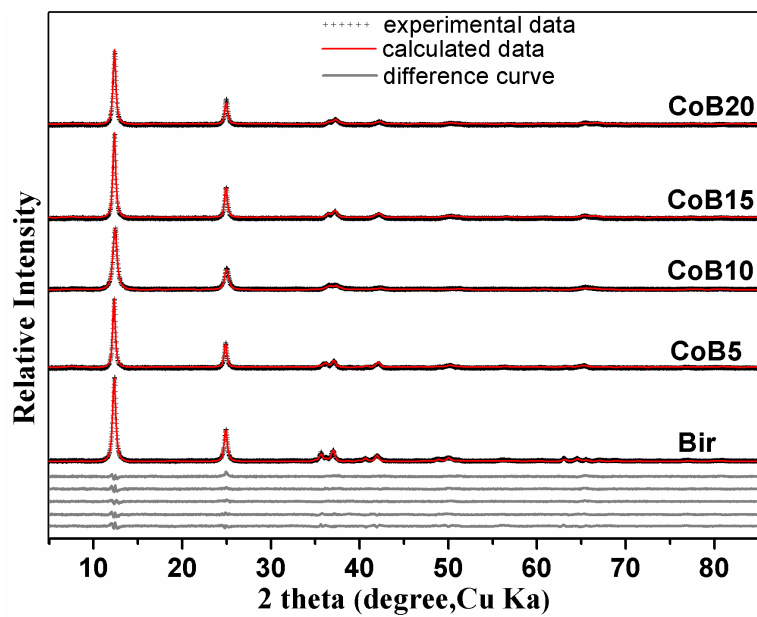


Fig. S2. Rietveld refinement of layered precursors. The gray lines at the bottom of the figure are difference curves for Bir, CoB5, CoB10, CoB15 and CoB20 from bottom to top.

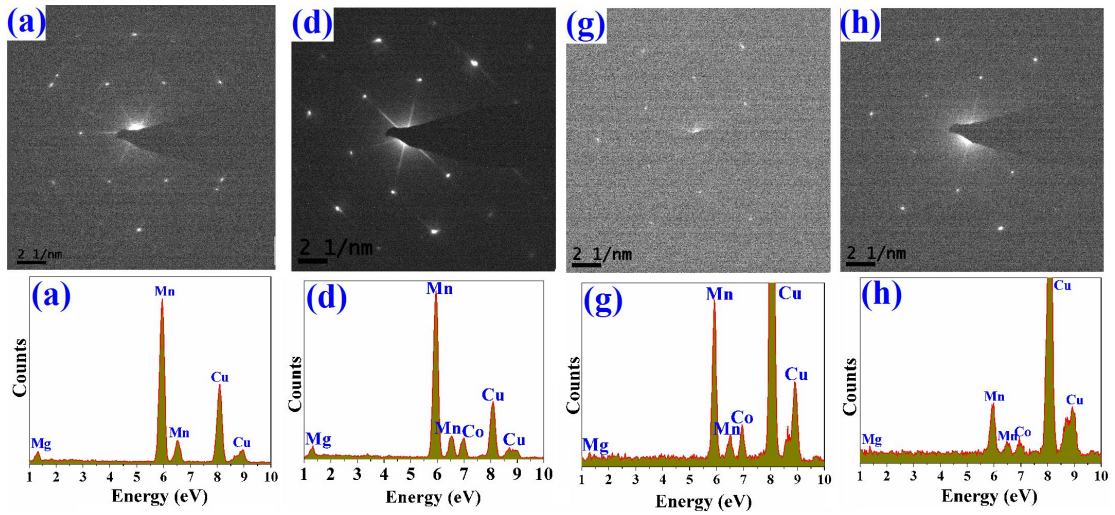


Fig. S3. Electron diffraction patterns (top) and energy-dispersive X-ray spectra (bottom) of reflux products: (a) Tod; (d) CoT5; (g) CoT15; (h) CoT20. Labels refer to individual particles shown on corresponding Fig. 8.

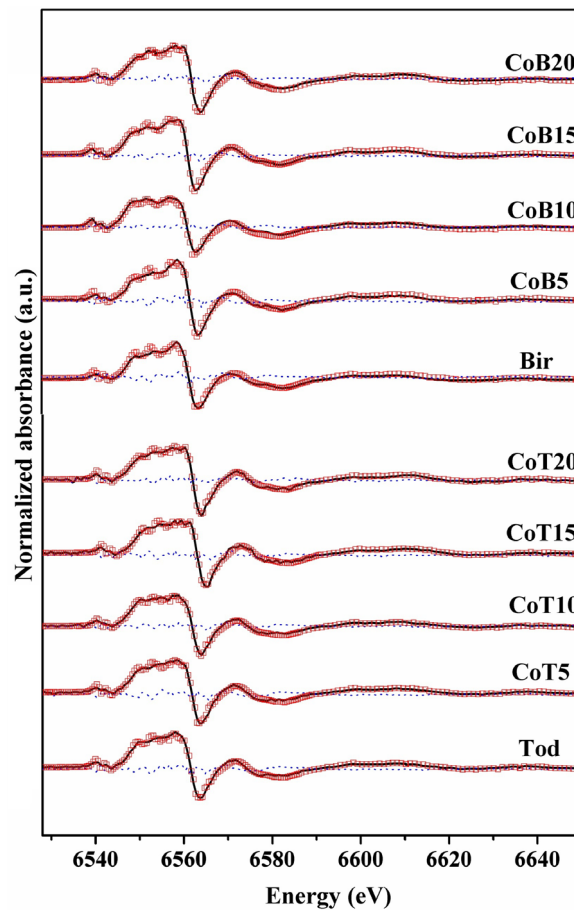


Fig. S4. Fit of the Mn K-edge XANES 1st derivative using the Combo method (Manceau et al., 2012). Squares, solid lines and dotted lines represent experimental data, best fits and residual. The references used to fit the data are those used by Manceau et al. (2012).

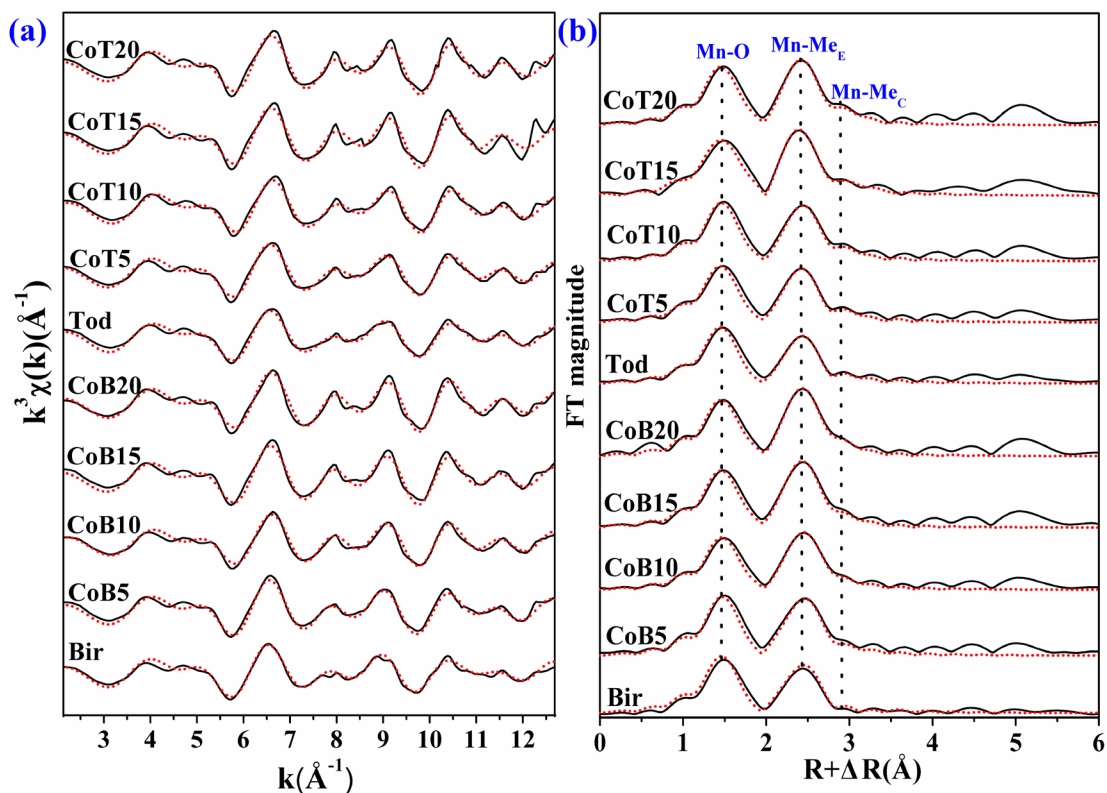


Fig. S5. Mn K-edge EXAFS spectra (a) and their Fourier transforms (b) for layered precursors and reflux products (solid black lines) with their best simulations overlaid (dotted red lines).

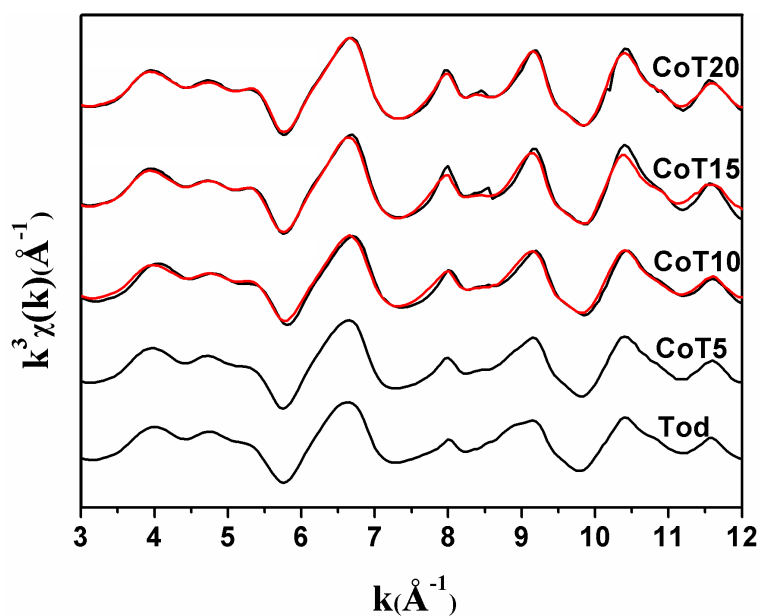


Fig. S6. Linear combination fits of Mn K-edge $\chi(k)$ EXAFS spectra for reflux products. Black and red solid lines are data and best fits, respectively. CoT5 and corresponding CoB spectra were used as reference compounds to determine the proportion of layered vs. tunnel and layered Mn oxides in the reflux products.

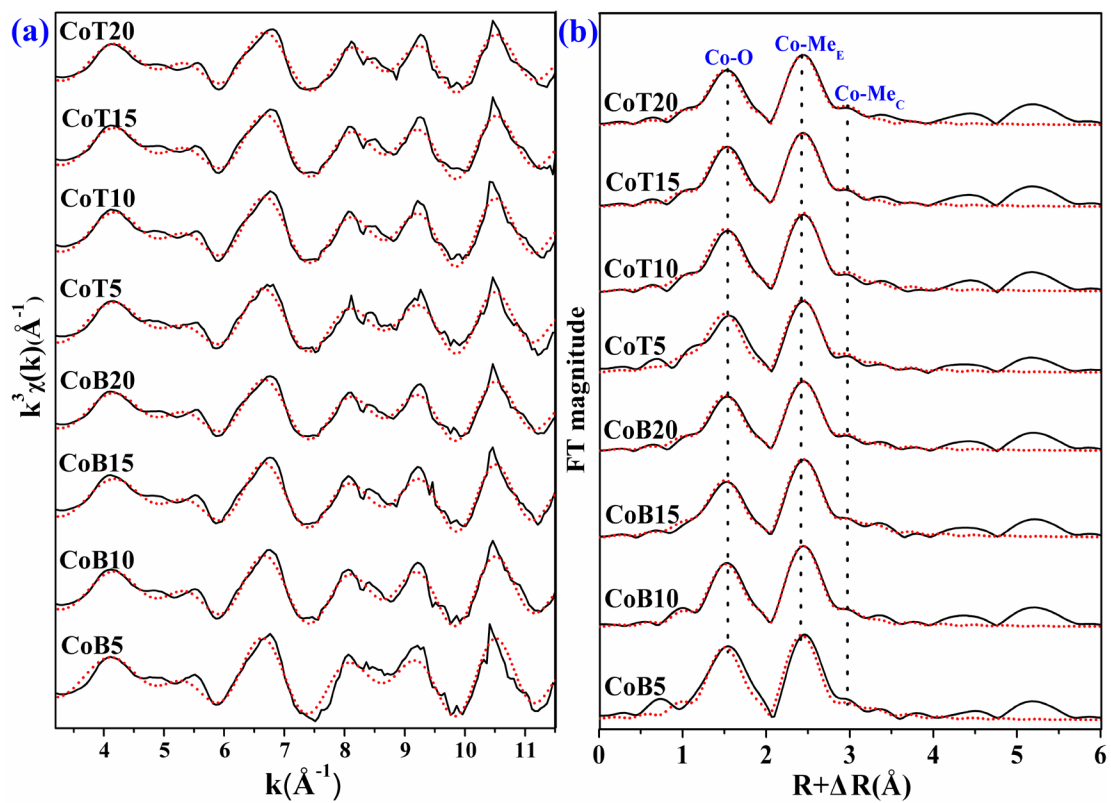


Fig. S7 Co K-edge EXAFS spectra (a) and their Fourier transforms (b) for layered precursors and reflux products (solid black lines) with their best simulations overlaid (dotted red lines).

Table S1.

Relative contributions of reference spectra to the best fits of Mn K-edge XANES first derivatives for layered precursors and reflux products shown in Fig. S4.

Samples	2-1	2-2	2-3	2-4	2-5	2-6	2-7	2-8	3-1	3-2	3-3	3-4	3-5	4-1	4-2	4-3	4-4	Total
Bir	n.d.	n.d.	0.7	n.d.	1.6	n.d.	n.d.	n.d.	n.d.	24.1	n.d.	n.d.	n.d.	14.3	n.d.	n.d.	51.9	92.6
CoB5	n.d.	n.d.	2.0	n.d.	0.5	n.d.	n.d.	n.d.	n.d.	15.5	n.d.	n.d.	n.d.	5.6	7.6	n.d.	62.4	93.5
CoB10	n.d.	n.d.	n.d.	n.d.	3.5	n.d.	0.4	n.d.	n.d.	23.7	n.d.	n.d.	0.3	1.4	13.6	n.d.	46.5	89.4
CoB15	n.d.	n.d.	2.5	n.d.	2.4	n.d.	n.d.	n.d.	n.d.	6.1	n.d.	n.d.	n.d.	n.d.	12.7	n.d.	68.9	92.5
CoB20	n.d.	n.d.	1.4	n.d.	3.3	n.d.	n.d.	n.d.	1.1	7.7	n.d.	n.d.	n.d.	n.d.	16.0	5.1	58.3	92.8
Tod	n.d.	n.d.	n.d.	n.d.	1.5	n.d.	n.d.	n.d.	n.d.	23.4	n.d.	n.d.	n.d.	3.3	11.8	5.0	50.5	95.6
CoT5	n.d.	n.d.	n.d.	n.d.	1.8	n.d.	n.d.	n.d.	n.d.	20.9	n.d.	n.d.	n.d.	n.d.	13.7	n.d.	54.8	91.1
CoT10	n.d.	n.d.	n.d.	n.d.	4.0	n.d.	n.d.	n.d.	n.d.	24.1	n.d.	n.d.	n.d.	2.7	10.5	6.0	45.6	92.9
CoT15	n.d.	n.d.	1.4	n.d.	n.d.	n.d.	n.d.	n.d.	11.2	n.d.	3.1	1.0	n.d.	n.d.	15.4	9.7	52.3	94.1
CoT20	n.d.	n.d.	1.7	n.d.	2.9	n.d.	n.d.	n.d.	6.7	0.5	n.d.	n.d.	n.d.	n.d.	14.8	11.6	56.2	94.5

The reference numbers are those of Manceau et al.(2012). n.d.: not detected